Assessing the impact of waves and platform dynamics on floating wind turbine energy production

Alessandro Fontanella[1], Giorgio Colpani[1], Marco De Pascali[1], Sara Muggiasca[1], and Marco Belloli[1]

[1]Mechanical Engineering Department, Politecnico di Milano, Milano, Via La Masa 1, 20156, Italy.

Correspondence: Alessandro Fontanella (alessandro.fontanella@polimi.it)

Abstract. Waves have the potential to increase the power output of a floating wind turbine forcing the rotor to move against wind. Starting from this observation, we use four multi-physics models of increasing complexity to investigate the role of waves and platform movements in the energy conversion process of four floating wind turbines of 5-15 MW in the Mediterranean Sea. The current technology of spar and semi-submersible floating wind turbines is not suitable to exploit the energy of waves because their design philosophy aims to minimize motions and structural loads, whereas large along-wind rotor movements are needed to increase the power output. Instead, in a realistic met-ocean environment, the power curve of the floating wind turbines we analyzed is lower than with a fixed foundation, with reductions of the annual energy production of 1.5-2.5%. The lower energy production is mainly ascribed to the platform static tilt, which reduces the rotor area projection on the vertical plane, and to floating-specific features of the turbine controller, that are thought to mitigate structural loading sacrificing power.

1 Introduction

Floating offshore wind turbines (FOWTs) have a high energy generation potential for deep waters. Compared to their bottom-fixed counterparts they can be installed in more sea areas and further away from the coast, where wind generally blows stronger, while reducing the visual impact from shore and interfering less with other users of the marine space. At the time of writing, the cost of energy produced by floating wind turbines is still high, but in the next decades it is expected to drop to the same level of other wind technologies (Wiser et al. (2021)).

One reason for the higher cost is that advantages of floating wind turbines are balanced by higher system complexity compared to bottom-fixed offshore wind turbines. The primary dissimilarity between the two technologies is the compliance of the floating foundation which allows large-amplitude low-frequency motions of the structure. Due to these motions, the rotor of a floating wind turbine may operate differently than when the tower is fixed to the seabed and it is reasonable to expect this has some effects on power production.

From an energy point of view, waves driving the floater motion introduce additional energy into the wind turbine which can potentially increase power generation. Finding ways to exploit waves energy in floating wind turbines has been identified as one research challenge for the wind energy community (van Kuik et al. (2016)). Few articles exist that study the impact of waves and platform dynamics on the power production of a floating wind turbine. Martini et al. (2016) investigated the effect of met-ocean conditions on tower inclination and hub acceleration and the possible consequences on shutdowns and capacity

factor. The influence of platform motion on the energy conversion process has been recently approached by Amaral et al. (2022) and Cottura et al. (2022), but both used simplifications such as prescribed sinusoidal movement of the platform in one direction and steady wind that make their findings difficult to apply to a real scenario.

Knowledge of the influence of waves and platform dynamics on the wind turbine energy production complements results of studies about the effect of wind and atmospheric conditions on the power output of land-based wind turbines. Among these, Clifton et al. (2014) discussed the impact of wind parameters on the performance of a wind turbine installed in a mountain pass with complex inflows, and St. Martin et al. (2016) explored the sensitivity of the power curve and annual energy production of a 1.5MW wind turbine to atmospheric conditions.

The fundamental question this article wants to answer is how the peculiar dynamics of floating foundations and wave excitation impact the energy production of a floating wind turbine. When answering this question, we examine four realistic wind turbine concepts of 5-15MW rating with spar and semi-submersible platforms and we consider the environmental conditions of an area in the Mediterranean sea suitable for the development of floating wind projects. The main contributions of this work are:

1. we use multi-fidelity models of increasing complexity to clarify how physics of the energy conversion process taking place in floating wind turbines is influenced by platform motion and waves;

2. we study the effect of floating wind turbine characteristics (control strategy, turbine rating, platform typology) and met-ocean conditions (wave spectrum, wind-wave directionality) on the generated power;

3. we define a methodology to introduce in multi-physics simulations of floating wind turbines the wind and waves conditions of a selected sea site. Wind and waves are described by a dataset measured by instruments normally used to characterize the met-ocean environment, such as anemometers and wave buoys.

Results and the methodology of this work can be leveraged in the early phase of floating wind projects to quantify their energy production and reduce the risk of investment. Better knowledge of the energy conversion process can help optimizing the turbines design for the operating conditions expected at a given sea area, thus lowering their cost. Moreover, in a future with high share of floating wind turbines, accurate knowledge of the power generated by these machines will be fundamental for electric grid management.

The structure of the article is as follows. Section 2 presents the four floating wind turbine concepts analyzed in this study, the numerical tools we used to estimate their energy production, the met-ocean conditions considered in the analysis, and the four simulation models. Section 3 reports the results of numerical simulations clarifying the influence of wind turbine control, platform compliance, dynamic platform motion, stochastic wind and waves on the power production of the four floating wind turbines. The article is concluded in Section 4 explaining possible uses of results obtained in this paper and reporting some suggestions for future work.

2 Methodology

A simple mathematical model is useful to understand the effect of platform motion on the energy production of a floating wind turbine. The aerodynamic power of the rotor is:

$$P_{\mathrm{r}} = \frac{1}{2}\rho C_P \pi R^2 V^3 \,, \tag{1}$$

where ρ is the air density, R the rotor radius, V the wind speed on the rotor, and C_P the power coefficient. The rotor of a floating wind turbine undergoes large motions allowed by the foundation compliance. Assuming this movement is harmonic and in the surge or pitch directions, we can replace the wind speed V with the apparent wind speed seen by the rotor V_{r} which is influenced by rotor moving against wind. If the wind field is uniform and steady:

$$V_{\mathrm{r}}(t) = U - \omega_{\mathrm{m}} A_{\mathrm{m,h}} \cos(\omega_{\mathrm{m}} t) \,, \tag{2}$$

where U is the mean wind speed, ω_{m} the motion circular frequency. $A_{\mathrm{m,h}}$ is the amplitude of the hub motion, in case of surge $A_{\mathrm{m,h}} = A_{\mathrm{m}}$ and in case of pitch $A_{\mathrm{m,h}} = A_{\mathrm{m}} h_{\mathrm{h}}$, where h_{h} is the hub distance from the tower base and A_{m} the amplitude of platform motion. $U_{\mathrm{r,h}} = \omega_{\mathrm{m}} A_{\mathrm{m,h}}$ is the amplitude of the apparent wind speed at the hub. Substituting Eq. 2 into Eq. 1:

$$P_{\mathrm{r}}(t) = \frac{1}{2}\rho C_P \pi R^2 \left(U^3 - 3U^2 U_{\mathrm{r,h}} \cos(\omega_{\mathrm{m}} t) + 3U \left(U_{\mathrm{r,h}} \cos(\omega_{\mathrm{m}} t) \right)^2 - \left(U_{\mathrm{r,h}} \cos(\omega_{\mathrm{m}} t) \right)^3 \right). \tag{3}$$

Looking at the four terms inside brackets on the left hand side of Eq. 3 we see that: U^3 is constant in time, $3U^2 U_{\mathrm{r,h}} \cos(\omega_{\mathrm{m}} t)$ has a null integral over one period of motion, the same is true for $3 \left(U_{\mathrm{r,h}} \cos(\omega_{\mathrm{m}} t) \right)^3$, but not for $U \left(U_{\mathrm{r,h}} \cos(\omega_{\mathrm{m}} t) \right)^2$. The mean value of rotor power over one period of motion is evaluated from Eq. 3 and it is:

$$\overline{P}_{\mathrm{r}} = \frac{1}{2}\rho C_P \pi R^2 \left(U^3 + \frac{3U U_{\mathrm{r,h}}^2}{2} \right). \tag{4}$$

Assuming C_P is constant in time, Eq. 4 shows that in a wind turbine experiencing harmonic platform surge motion the mean power available at rotor is higher than with a fixed foundation. It has to be seen if the power increment predicted by this simple model translates into higher generated power also in normal operating conditions. In fact, the rotor C_P is not constant but it is modified dynamically by the wind turbine controller; moreover, the motion of a floating turbine is not perfectly aligned to the wind, but its direction depends on the directionality of wind and waves and on platform characteristics.

In this work, we assume the energy production of a floating wind turbine is influenced by:

- wind, described by mean wind speed, mean direction, turbulence intensity, and vertical shear.

- wave, described by elevation, period, and direction.

- floater characteristics such as restoring, static stability, dynamic response to environmental loads.

- turbine control strategy, which is modified to accomodate large low-frequency motions permitted by floating foundations and constitutes a key element of difference between floating and bottom-fixed wind turbines (van der Veen et al. (2012)).

In order to isolate their effect, we introduce gradually these parameters in the analysis.

2.1 Simulation scenarios and tools

The impact of waves and platform dynamics on power production is studied with four multi-fidelity models of the floating wind turbine and of the wind-wave conditions around it. The four models gradually add complexity to the simple analytical model of Eq. 3 as it is shown schematically in Fig. 1. In detail:

90   – The Harm-M model extends the results of Eq. 3 using a more accurate representation of the wind turbine and its control system. The rotor aerodynamic response is calculated with a non-linear engineering model rather with a constant power coefficient, blades and tower are flexible elements and the wind turbine is regulated with an active control scheme. The wind turbine is subjected to prescribed platform motion of harmonic type in the surge, sway, heave, roll, pitch, and yaw directions; wind is steady and uniform.

95   – The Harm-W model introduces in the analysis the hydrodynamic loading and the floater dynamic response to waves; waves are of regular type and can have a different direction than wind.

      – In the Coupled-S model, wind and wave properties are defined according to the standard industrial practice to reflect the met-ocean conditions of a sea area in the Mediterranean; wind and waves are aligned to the platform main axis and excite motion of the rotor in the along wind direction, as in Eq. 3.

100   – In the Coupled-C model, the environmental conditions are extracted by means of a clustering algorithm from a database of met-ocean data recorded at the site of reference. In Coupled-C simulations wind and waves are not aligned, but their directionality is representative of the portion of sea of our interest. In this work, the Coupled-C scenario is the most accurate representation of conditions a floating wind turbine would meet if installed in the area we selected.

The modeling approaches for wind, waves and floating platform of the four simulation scenarios are summarized in Table 1.

Table 1. Comparison of modeling approaches for wind, waves, and floating platform in the four simulation scenarios. Wind and waves are "Aligned" when they are directed along the platform main axis.

Model	Floating platform	Wind	Wind direction	Wave	Wave direction
Harm-M	No, prescribed motion	Steady, unsheared	Aligned	No	–
Harm-W	Spar, semi-submersible	Steady, unsheared	Variable	Regular	Variable
Coupled-S	Spar, semi-submersible	Turbulent, vertical shear	Variable	Regular	Variable
Coupled-C	Spar, semi-submersible	Turbulent, vertical shear	Variable	Regular	Variable

105   The Harm-W and Coupled-C models consider the wind-wave directionality. The wind and waves heading directions (θ and β, respectively) are defined in Fig. 2; their difference $\gamma = \theta - \beta$ is the wind-wave misalignment angle. We assume the nacelle yaw angle is always consistent with the wind direction.
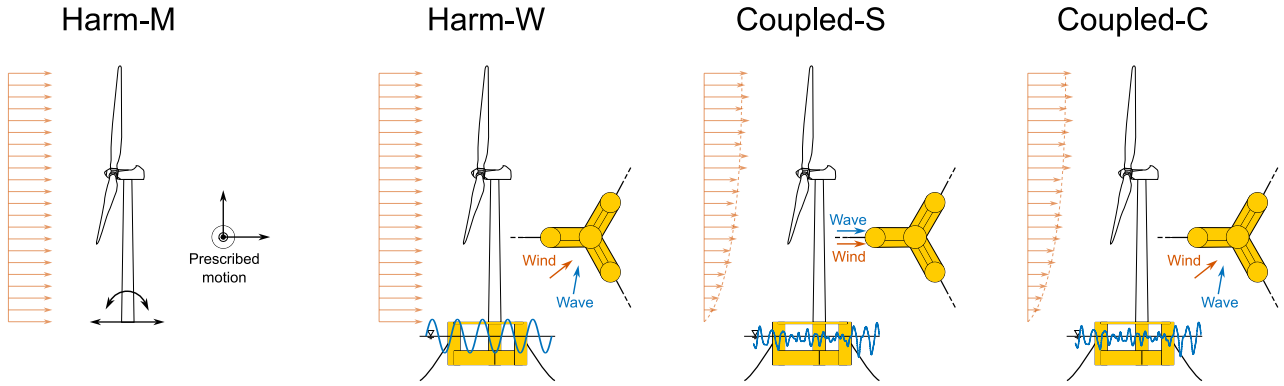
Figure 1. The influence of platform motion due to waves on the power production of floating wind turbines is studied with four simulation scenarios. In the Harm-M case, sinusoidal motion of varying amplitude and frequency is prescribed at the wind turbine tower base. In the Harm-W simulations, the turbine is excited with regular waves of different amplitudes, frequencies and directions. In the coupled simulations, the wind turbine response is computed for several environmental conditions with full-field turbulent wind and irregular waves; wind-wave conditions are obtained with simplifications typically used by standards (Coupled-S) or they are extracted by means of clustering from a database of met-ocean data (Coupled-C).
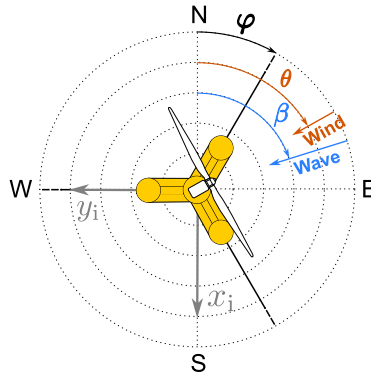

Figure 2. Definition of the platform mounting orientation (φ), of the wind direction (θ), the wave direction (β), and the wind-wave misalignment angle ($\gamma = \theta - \beta$). x_i and y_i are the axes of the earth-fixed coordinate system.

All models are built in OpenFAST (Jonkman et al. (2023)), which includes modules for aerodynamics, hydrodynamics, control, and structural dynamics. The aerodynamic forces are calculated in AeroDyn v15 based on the quasi-steady blade element momentum theory. The aerodynamic influence of the tower is accounted with a potential flow model and the blade airfoil aerodynamics is computed using the Beddos-Leishman model. The structural response of the system is modeled in ElastoDyn based on the modal approach. Hydrodynamic forces are calculated in HydroDyn using a combination of potential-flow theory and strip-theory solution; the hydrodynamic coefficients required for the potential-flow solution are obtained with a

panel code. The mooring lines are modeled in MoorDyn which uses a lumped-mass approach to discretize the cable dynamics over the length of the lines (Hall and Goupee (2015)). In Harm-M cases, tower-base motion is prescribed replacing the floating platform with a mass-spring-damper system implemented in the SubDyn module (Branlard et al. (2020)).

The incoming turbulent wind is introduced in the simulations by means of TurbSim (Jonkman (2009a)), which is a stochastic, full-field, turbulent wind simulator using a statistical model to numerically simulate the time series of the three components of the wind velocity vector at specified points of a two-dimensional grid fixed in space.

2.1.1 Simulations with prescribed motion

In this scenario platform motion is prescribed at tower base, it is sinusoidal and along one of the six rigid-body motion directions of the turbine foundation. The motion frequency ranges from 0 Hz to 0.3 Hz; the motion amplitude varies from 0 m to 3 m in case of translations, and from $0°$ to $1.25°$ in case of rotations; wind is steady and has no shear. This assumption is unrealistic but enables us to discern more clearly the effect of platform motions on the generated power.

2.1.2 Simulations with regular waves

The Harm-W scenario is similar to the Harm-M, but introduces in the analysis the dynamic response of the floating wind turbine to incident wave. Wave is of regular type and has variable direction β; the values of wave height are 0.5 m, 1.0 m, 1.5 m, 2.0 m, 2.5 m, 3.0 m; the values of wave frequency are 0.05 Hz, 0.10 Hz, 0.15 Hz, 0.20 Hz, 0.25 Hz, 0.30 Hz. These values are representative of the wave conditions at the sea site of reference, described in Sect. 2.3. Wind is steady and has no shear.

2.1.3 Coupled simulation with simplified wind-wave conditions

The Coupled-S model uses stochastic sheared wind and stochastic waves. The load cases are defined according to the recommendations of IEC 61400-3 (International Electrotechnical Commission (2019)) for fatigue load calculations:

– wind and wave are aligned to the platform symmetry axis (i.e., with reference to Fig. 2, $\varphi = \beta = \theta = 0°$);

– a wind speed interval of 2 m/s is considered starting from 3 m/s and up to 25 m/s;

– the wave height is defined from its linear correlation with the average wind speed;

– three wave periods are associated to each wave height. Wave periods are obtained from the scatter diagram of the site as the three most probable for the selected wave height.

Every load case is simulated for 3 hours.

2.1.4 Coupled simulation with clustered wind-wave conditions

Coupled-C simulations reproduce the wind-wave environment of the sea site of reference without making use of assumptions on the relations among wind speed, wind direction, wave height, wave period, and wave direction. Instead, the load cases of simulations are extracted from long-term series of the wind and wave parameters.

Approximately 4 CPU hours are required to simulate in OpenFAST one sea state for 3 hours, and it is unpractical to simulate a dataset covering several months or years. Thus, the Coupled-C model considers a small subset of conditions that are representative of the long-term sea conditions at the site. The selection procedure is based on the data-clustering technique, which aims to extract features from the original dataset giving a more compact representation of the dataset properties. Data clustering has seen application in the wave climate analysis (Camus et al. (2011)) and to extrapolate wind statistics needed to estimate the energy production of wind energy systems (Schelbergen et al. (2020)).

Here, the selection of the subset of met-ocean conditions is based on the K-means algorithm (KMA) (Arthur and Vassilvitskii (2007)). The initial database is formed by five-dimensional vectors, whose elements are the variables of interest that characterize the wind and wave climate: wind speed (U), wind direction (β), wave significant height (H_s), wave peak period (T_p), and wave direction (θ).

Given the initial database of N five-dimensional vectors $\mathbf{x}^i = \{U_i, \beta_i, H_{\mathrm{s},i}, T_{\mathrm{p},i}, \theta_i\}$ with $i = 1, \ldots, N$, the KMA identifies M groups of data, each defined by a five-dimensional prototype $\mathbf{v}^k$ with $k = 1, \ldots, M$ called centroid. The clustering procedure starts with a random initialization of the M centroids; on each algorithm iteration, the nearest data to each centroid are identified and the centroid is redefined as the mean of the corresponding data. For example, on the $(r+1)$ step, a data vector $\mathbf{x}^i$ is assigned to the group $j|\{\min\|\mathbf{x}^i - \mathbf{v}_r^j\|, j = 1, \ldots, M\}$, where $\|\cdot\|$ is the Euclidean distance, and $\mathbf{v}_r^j$ is the j-th centroid at the r-th step. Once every data vector is assigned to a group, the centroid is updated as:

$$\mathbf{v}_r^j = \sum_{\mathbf{x}^i \in C^j} \frac{\mathbf{x}^i}{n_j} = 1, \tag{5}$$

where n_j is the number of elements of the j-th group and C^j is the subset of data included in the group j. The KMA iteratively moves the centroids minimizing the overall within-cluster distance until it converges and data belonging to every group are stabilized. The working principle of the clustering algorithm is showcased in Appendix A using the dataset of the sea site of reference of this study, that is presented in Sect. 2.3.

The number of clusters representing the sea states is a trade-off between the computational cost required to simulate them and the error committed in using a subset of data instead of the complete dataset. Here, the number of clusters is fixed to $M = 36$, which is the same number of conditions considered in the Coupled-S simulations. Every load case is simulated for 3 hours.

2.2 Floating wind turbines concepts

The wind turbines of the FOWTs concepts are the NREL 5 MW (Jonkman et al. (2009)) and the IEA 15 MW (Gaertner et al. (2020)) which key parameters are summarized in Table 2.

Table 2. Key properties of the NREL 5 MW and IEA 15 MW wind turbines.

Parameter	Unit	NREL 5 MW	IEA 15 MW
Power rating	MW	5	15
Cut-in wind speed	m/s	3	3
Rated wind speed	m/s	11.4	10.59
Cut-out wind speed	m/s	25	25
Design tip-speed ratio	-	7.55	9
Minimum rotor speed	rpm	-	5
Rated rotor speed	rpm	12	7.56
Rotor diameter	m	126	240
Hub height	m	90	150

The two wind turbines have a conventional variable-speed, variable blade-pitch-to-feather configuration. Power-production operation is controlled with the Reference OpenSource Controller (ROSCO) of Abbas et al. (2022) (version 2.8.0, NREL (2023a)) which is deemed to be representative of controllers adopted in commercial multi-megawatt wind turbines. In ROSCO, two active proportional integral (PI) controllers are implemented for generator torque and collective blade pitch angle. Saturation limits on rotors speed and blade pitch are used to ensure the turbine works within its design limits. ROSCO has two operating regions:

- below rated wind speed. Blade pitch is fixed to its design value of $0°$, and a PI controller regulates the generator torque to track the design tip-speed ratio (TSR). The IEA 15 MW has a minimum rotors speed constraint of 5 rpm, thus at low wind speed the blade pitch is scheduled based on a wind speed estimate to improve the turbine power output. This functionality is not used in the NREL 5 MW. The estimate of rotor-effective wind speed required by the TSR-tracking controller and the pitch scheduling is provided by an extended Kalman-filter estimator.

- above rated wind speed. Generator torque is constant and equal to its rated value and rotor speed is regulated with a PI controller on the collective blade pitch angle.

The controllers settings we adopted are those of the reference OpenFAST models of the four floating wind turbines and no further tuning was done in this study.

In addition to these baseline control strategies, we used two more advanced ROSCO functionalities:

- peak shaving. This algorithm reduces the maximum thrust force reached when the turbine operates in near-rated winds. The peak shaving is implemented prescribing a minimum blade pitch $> 0°$ function of the wind speed.

- nacelle velocity feedback. In above rated wind speed, the nacelle fore-aft acceleration is band-pass filtered, integrated, and multiplied by a constant gain which is set with the method of Abbas et al. (2022). The blade pitch command obtained

with this algorithm is summed to the output of the PI pitch controller for rotor speed to improve stability of platform motion.

We avoided using any control algorithm for start-up and shut-down sequences. When wind speed is below cut-in or above cut-out, the wind turbine is stopped and does not produce any power. Moreover, there is no control action to regulate the nacelle-yaw angle which is assumed to be constant.

We expect these control strategies will be used in future floating wind turbines. The peak shaving is increasingly important for large FOWTs because it lessens the restoring requirements of the floating platform (Renan dos Santos et al. (2022)). Traditionally, the instability issues of FOWT controllers have been solved with detuning, i.e., reducing their bandwidth below the platform pitch natural frequency (van der Veen et al. (2012)). As the FOWT size increases, the platform natural frequencies decrease leading to slower controllers when applying detuning. This is avoided with nacelle velocity feedback that improves power quality while reducing structural loads (Fleming et al. (2019),Vanelli et al. (2022)).

The steady-state operating points of the NREL 5 MW and IEA 15 MW with fixed tower base regulated with the control strategies described above are visualized in Fig. 3.
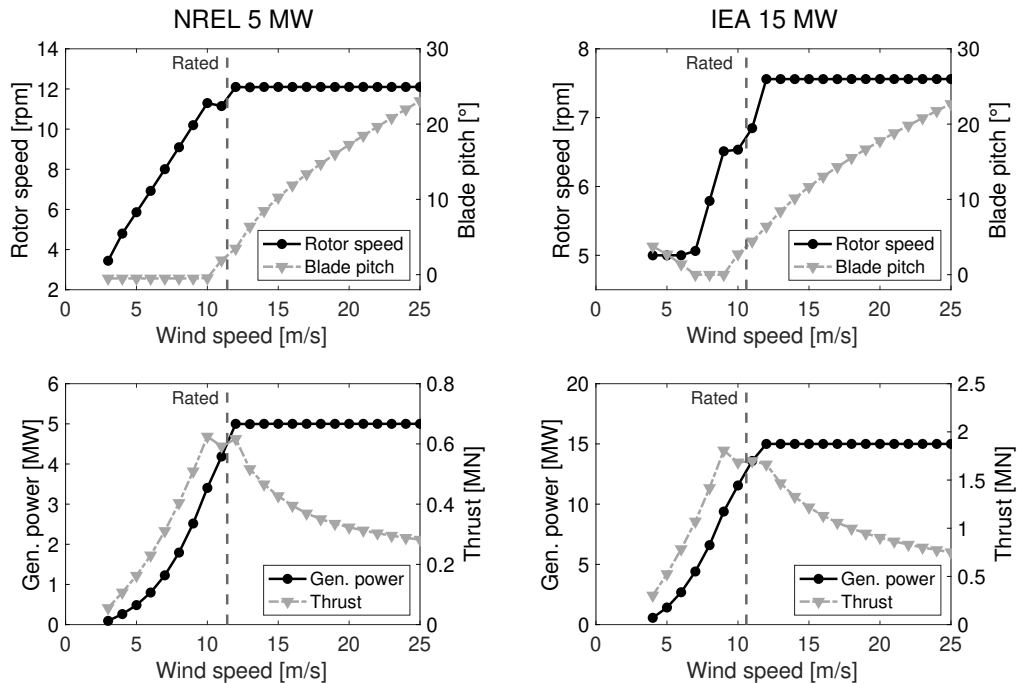
Figure 3. Steady-state operating points of the land-based version of the NREL 5 MW and IEA 15 MW wind turbines.

Two platform concepts are examined for each wind turbine: a spar-buoy and a semi-submersible. We decided to focus on these substructures typologies because they have been adopted in recent commercial projects and research works. Moreover, there are OpenFAST models easily accessible in online repositories.

2.2.1 VolturnUS 15 MW semi-submersible

The UMaine (University of Maine) VolturnuUS-S (Allen et al. (2020)) is an open-source concept of a semi-submersible floating wind turbine based on the IEA 15 MW. The floater is made of steel and is composed of three 12.5 m diameter columns disposed symmetrically around a central column hosting the wind turbine. The three bottom pontoons connecting the inner and outer columns have a rectangular section (12.5 $\times$ 7.0 m); three cylindrical struts connect the top of the outer column to the central one. The operational draft of the floater is 20 m; the total mass of the platform is 17854 t. The mooring system is designed for a generic 200-m-depth location and is composed of three 850 m long chain-catenary lines, arranged at 120° angle around the floater. The fairlead is located at the extreme point of each external column, at a radius of 58 m from the vertical axis of the floater and 14 m below the sea water level. The OpenFAST model of the VolturnUS is available from Allen et al. (2023).

2.2.2 WindCrete 15 MW spar

The WindCrete, introduced by Campos et al. (2016), is a spar-type platform supporting the IEA 15 MW. The tower and the spar form a monolithic structure made of concrete. The spar has a diameter of 18.6 m, a draft of 155 m, and has ballast in its lower section to increase the hydrostatic stiffness in the roll and pitch directions. The tower has conical shape and, in the version of Campos et al. (2016), it places the hub 135 m above the mean sea level. We increased the tower base height from 15 m to 30 m keeping the same tower flexible length to have the same hub height of the VolturnUS of 150 m. Due to this change, the first fore-aft natural frequency is 0.57 Hz instead of 0.5 Hz of the original tower. The mooring system consists of three catenary lines attached to the platform hull with delta-shaped connections. The global response of the WindCrete to several wind and wave conditions is examined by Mahfouz et al. (2021) and the OpenFAST model of the platform is published in the repository of Molins et al. (2020).

2.2.3 DeepCwind 5 MW semi-submersible

The OC4 DeepCwind semi-submersible is a floater design developed in the DeepCwind project (Robertson et al. (2014)). The platform consists of a main column supporting the wind turbine tower and three offset columns connected to the main one through a series of smaller diameter pontoons and cross members; the draft is 20 m. The floater is moored with three catenary lines spread symmetrically about the vertical axis. The fairleads are positioned at a depth of 14.0 m below the water level, at a radius of 40.87 m from the platform centerline, while the anchors are located at a water depth of 200 m and at a radius of 837.6 m from the platform centerline.

2.2.4 OC3 5 MW spar

The OC3-Hywind spar-buoy is a floater designed for the NREL 5 MW reference wind turbine (Jonkman (2009b)). The floater is made of steel, ballasted with inert material, and it is composed of a 120 m draft cylinder of 9.4 m diameter, tapered to 6.5 m diameter in correspondence of the sea surface. The linearly tapered conical region extends from a depth of 4 m to a depth of 12 m below the mean sea level; the overall length of the floater is 130 m. The design water depth for the floater is 320 m. The

mooring system consists of three all-chain slack catenaries, spread 120° apart; each line has an unstretched length of 902.2 m and a diameter of 0.09 m; a delta line connecting mooring lines to fairleads is used to increase yaw stiffness.

2.3 Reference sea site and met-ocean conditions

The wind and wave conditions defining the load cases are representative of the climate at a sea area sited in the Golf de Fos, located off the French coast in the Mediterranean sea. The site of reference is shown in Fig. 4, it is 40 km offshore Fos Sure Mer and its approximate location is identified by the coordinates Lat. 43°6'15.12"N, Long. 4°44'32.06"E.
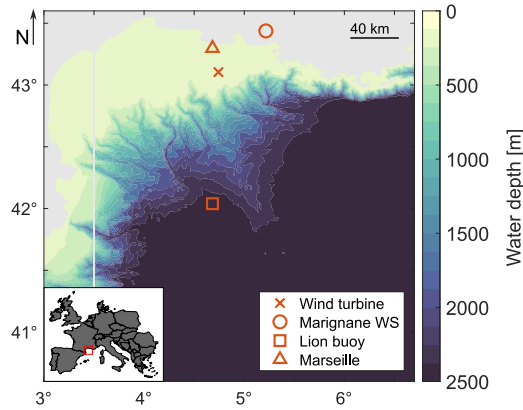
Figure 4. Sea area of the reference site of this study. The area is located in the Mediterranean sea off the French coast, as shown in the inset map. Markers show the position of the floating wind turbine, the Marignane Weather Station, the Lion Buoy, and the city of Marseille. Land is depicted in gray and the color scale corresponds to water depth (EMODnet (2023)).

Two open-access databases have been used to characterize the wind and wave conditions at this site: wind data of the Marignane Weather Station, provided by Meteostat (Meteostat (2022)); wave data of the Gulf of Lion buoy, located 100 km south to the site location, shared by MetoFrance (France (2022)). The variables of interest for this study are: wind speed at 10 m height, wind direction, wave elevation, wave period, wave direction. The two databases contain wind-wave measurements for several years, however, wave directionality measurements are available only for a period of six months, from October 2019 to March 2019. The time resolution is 1 hour and the dataset with simultaneous information about the five variables of interest has 3362 data points in total.

No information about the vertical profile of mean wind speed is available, thus it is assumed to follow the power law:

$$U(z) = U(h)\left(\frac{z}{h}\right)^{\alpha},$$ (6)

where U is the mean wind speed, z a generic height, h is the reference height of 10 m, and α is the shear exponent. In accordance with the meteorological study of Krieger et al. (2015) we take $\alpha = 0.14$.

11

255   The wind speed distribution is essential for evaluating the wind turbine annual energy production. Figure 5 shows the probability density function of the 1-hour mean wind speed extrapolated at 150 m height (i.e., the hub height of the IEA 15 MW) by means of Eq. 6. The best fitting Weibull distribution has scale parameter of 7.17 and shape parameter of 1.38. The probability of occurrence of wind speed is over predicted in some bins (e.g., 5-6 m/s, 8-9 m/s), and this problem is likely due to the small size of the database. The best fitting Weibull distribution for the 1-hour mean wind speed at the hub height of the NREL 5 MW (90 m) has scale parameter of 6.68 and shape parameter of 1.38.
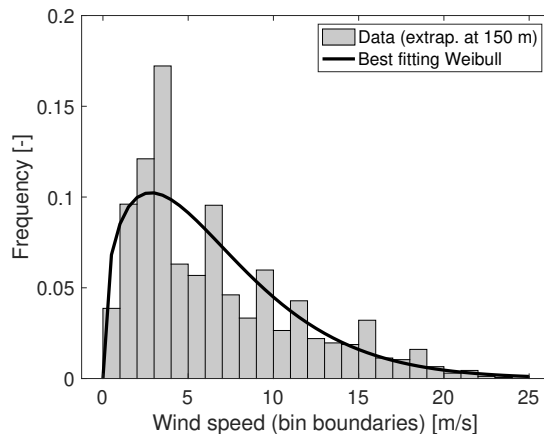
Figure 5. Probability density function of the 1-hour mean wind speed at 150 m at Marignane Weather Station obtained from data recorded between October 2019 and March 2019. The best fitting Weibull distribution is obtained for scale parameter of 7.17 and shape parameter of 1.38.

260

      There is no measurement of turbulence intensity at the site, thus the Normal Turbulence Model (NTM) is used. The characteristic standard deviation of wind speed is given by:

$$\sigma_u = I_{\mathrm{ref}}(0.75 U_{150} + 5.6), \tag{7}$$

where U_{150} is the mean wind speed at 150 m, and $I_{\mathrm{ref}} = 0.12$ which is appropriate for onshore Class C turbines and conservative

265   for offshore turbines of similar characteristics.

      Figure 6 shows the wind rose from the records, where wind speeds were extrapolated to their value at 150 m by means of Eq. 6, and the rose of the wave coming-from direction. Waves come from SE most of the time, while it is equally probable to have wind from SE and NW, suggesting the assumption of wind-wave alignment is not representative of this site.

      In the Coupled-S model, wave elevation H_{s} is assumed to depend linearly on wind speed:

270   $$H_{\mathrm{s}} = 0.128 U_{150} + 0.844. \tag{8}$$

Coefficients in the expression were obtained from linear regression of wave height and 150 m-mean wind speed data.

      The wind-wave conditions of the Coupled-S simulations for the Golf de Fos site are reported in Table B1. Environmental conditions of the Coupled-C simulations are obtained applying the clustering algorithm of Sect. 2.1.4 to the dataset of five-
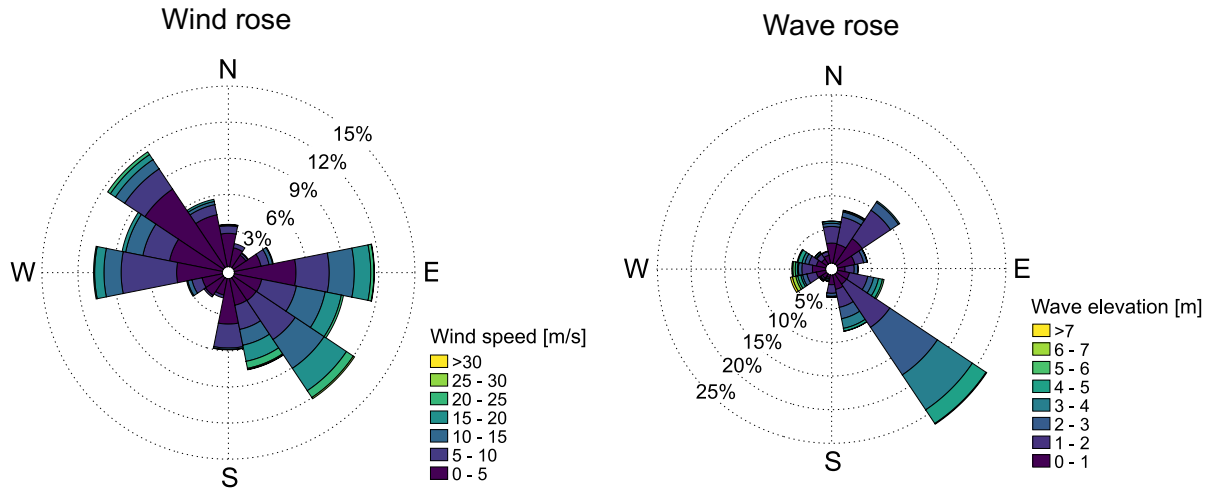
Figure 6. Wind rose of the 1-hour wind speed at 150 m and wave rose of the 1-hour wave elevation.

dimensional vectors $\mathbf{x}^i = \{U_i, \beta_i, H_{s,i}, T_{p,i}, \theta_i\}$ with $i = 1, \ldots, 3362$. The 36 conditions identified by the clustering algorithm are reported in Table B2.

3 Results

In this section we show the results of the four simulation scenarios described in Sect. 2.1. Key parameters to analyze the impact of waves and platform motions on the wind turbine energy production are the time-average value of the generated power ($\overline{P_g}$), the wind turbine power curve function of wind speed, and the annual energy production (AEP). Before reporting the results of the Harm-M, Harm-W, Coupled-S and Coupled-C simulations, we show the influence on the wind turbine power curve of the peak shaving control strategy and platform static tilt (Sect. 3.1) and of wind shear and turbulence (Sect. 3.2).

3.1 Influence of peak shaving control and platform static tilt

Figure 7 shows how the power curve of the NREL 5 MW and the IEA 15 MW with steady non-sheared wind changes due to the use of a peak-shaving routine in the wind turbine controller and due to a floating foundation compared to a bottom-fixed one. The peak shaving routine reduces the turbine power near the rated wind speed because the turbine does not work at the power-optimal operating point when blade pitch is different than the fine pitch. This reduction is up to 8.9% for the NREL 5 MW and 11% for the IEA 15 MW.

When the turbine is on top of a floating foundation, the thrust force results in a static tilt rotation of the structure and a reduction of the rotor area projection on the vertical plane. The four floating wind turbines have a maximum static tilt between 3-4° near the rated wind speed and the consequent maximum reduction of the generated power is around 3%.
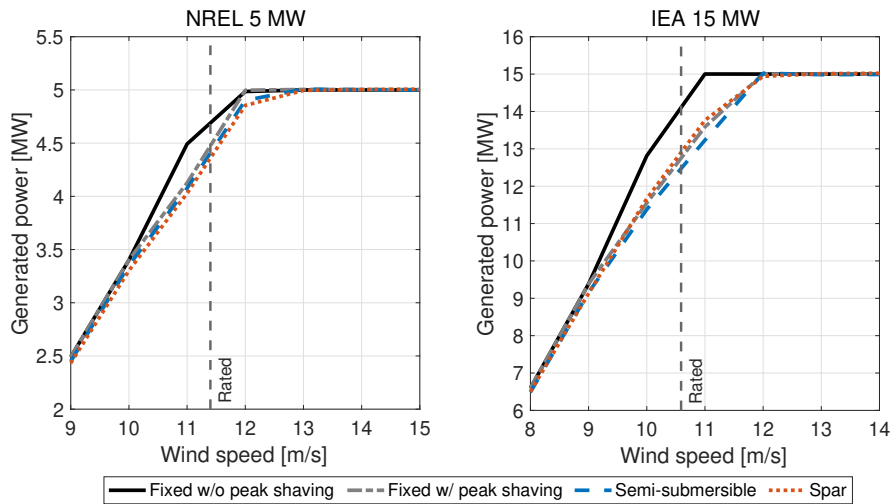
13

Figure 7. Steady-state power curves of the NREL 5 MW and IEA 15 MW wind turbines with a fixed, a semi-submersible, and a spar foundations. The power curve near the rated wind speed is influenced by the peak shaving control strategy, which reduces the conversion efficiency making the turbine work far from its aerodynamically-optimal operating point, and the use of a floating foundation, which is responsible of a large rotor tilt angle and a consequent reduction of the rotor area projection on the plane normal to wind. Peak shaving is used in all floating wind turbines.

3.2 Influence of wind shear and turbulence

The met-ocean database at our disposal does not provide any information about the vertical profile of mean wind speed and turbulence intensity, therefore wind shear and turbulence in Coupled-S and Coupled-C simulations have been selected based on standards. This procedure is common in the early stage of floating offshore wind projects when detailed measurements of
295   wind parameters at a given site are not available.

Sensitivity to wind shear is assessed from the power curve with steady wind and no waves. The wind speed vertical profile is obtained with Eq. 6 fixing the reference height at the wind turbine hub and changing the shear exponent α. Figure 8 shows how the power curve of the four floating wind turbines changes for several values of α. The shear exponent influences the wind turbine power curve in the below rated region: the rotor-averaged wind speed decreases for higher values of α and the turbine
300   produces less power; above the rated wind speed, the turbine power is saturated and it is not affected by α.

Sensitivity to turbulence intensity is evaluated simulating the wind turbine with no waves, the wind speeds of Table B1 and changing I_{ref} in the NTM of Eq. 7. Every wind condition was simulated for 3 hours. In Fig. 9 we see that in the case with $I_{ref} = 0.06$ the power is lower than with steady wind for below-rated wind speeds. A further increase in turbulence brings higher power near cut-in and lower power close to rated. As explained by St. Martin et al. (2016), near the rated wind speed,
305   the turbine controller acts on the blades pitch to counteract rotor overspeed driven by wind gusts. Since the controller does not react instantly to rotor speed and blade pitch cannot go below $0°$, the average blade pitch with turbulence and a near-rated wind speed is different from its power-optimal value which is instead used in the steady wind case.
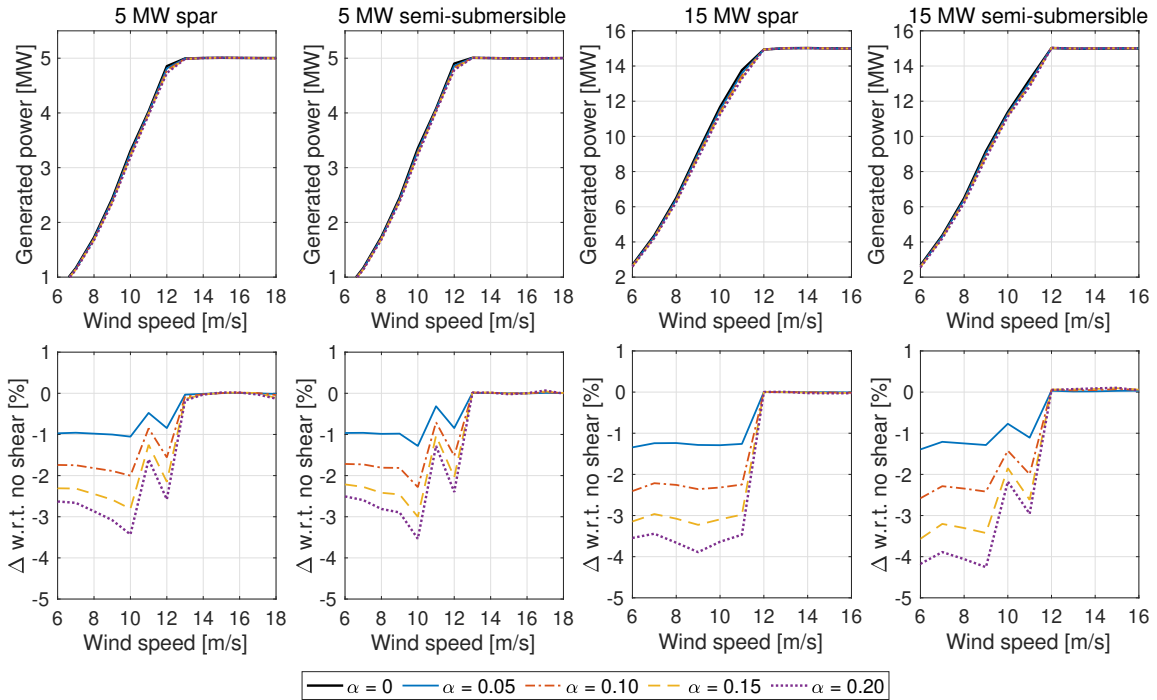
14

Figure 8. Sensitivity to wind shear of the four floating wind turbines. Power curves and percent variation of the power curve with respect to the case with no shear ($\alpha = 0$).

We estimate that uncertainty in wind shear and turbulence intensity may result in variations of the power curve up to 10%. Uncertainty in the power curve due to wind characteristics is mostly in the below rated region.

310 **3.3 Power response to prescribed platform motion**

To begin the discussion of Harm-M simulations results and to make a contact point with the analytical model of Eq. 3-4, in Fig. 10 we show the time series of power generated by the IEA 15 MW, with prescribed surge motion of 1.5 m amplitude and 0.2 Hz frequency. Two steady-uniform wind conditions are examined, one in the below-rated region with a wind speed of 9 m/s, and one with an above-rated wind speed of 15 m/s. In the 9 m/s case, the land-based turbine has an average production

315 of 9.4 MW, which is increased to 10.1 MW when the platform undergoes harmonic surge motion (+7.5%). In the above rated operating condition, motion has a lower influence on the power production that passes from 15 MW of the land-based turbine to 14.9 MW when the platform moves (-1%).

Figure 11 shows $\overline{P_\mathrm{g}}$ of the NREL 5 MW and the IEA 15 MW computed from results of Harm-M simulations with surge and pitch motions and a wind speed of 9 m/s. In Fig. 11 $\overline{P_\mathrm{g}}$ is normalized by the turbine power with no prescribed motion. The

320 average power output increases with increasing frequency and amplitude of platform motion. Movements in the surge or pitch directions give an apparent wind at the rotor, which causes an increase in generated power as explained in the analytical model
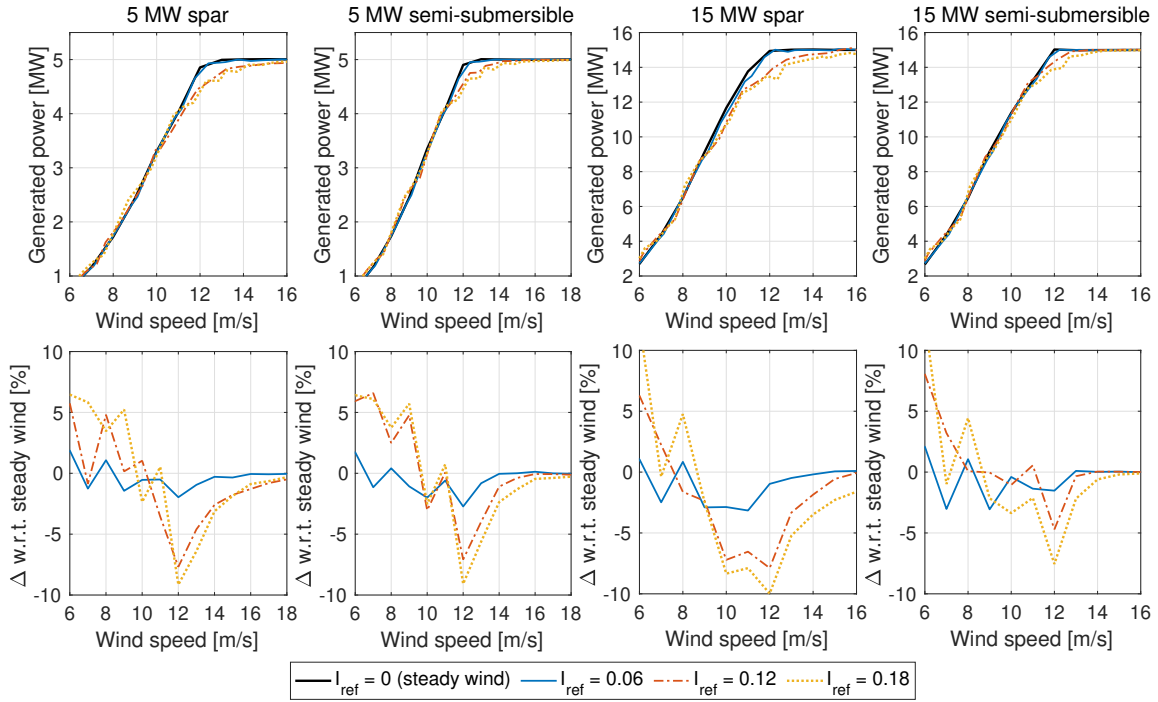
Figure 9. Sensitivity to wind shear of the four floating wind turbines. Power curves and percent variation of the power curve with respect to the case with steady wind.
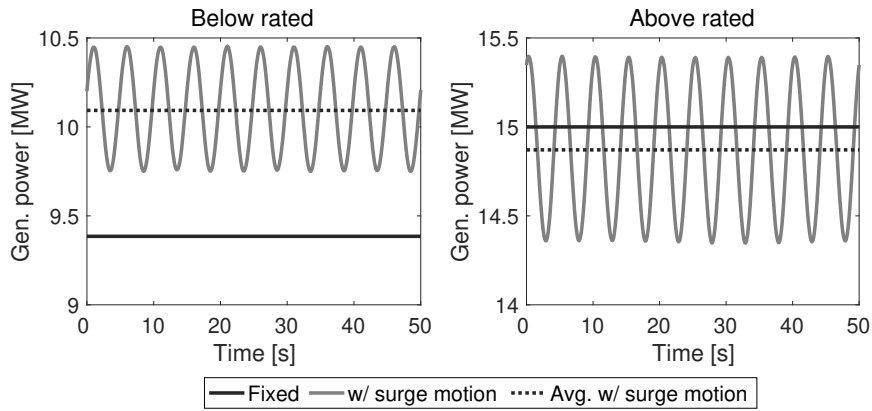

Figure 10. Power generated by the IEA 15 MW with a below-rated wind speed of 9 m/s and an above-rated wind speed of 15 m/s, with fixed tower bottom and with prescribed platform surge motion of 1.5 m amplitude and 0.2 Hz frequency.

of Eq. 3. The power increment is proportional to the amplitude of the apparent wind speed variations at hub, which is equal to $U_{r,h} = \omega_m A_m$ in case of surge and $U_{r,h} = \omega_m A_m h_h$ in case of pitch. In the surge case the apparent wind is uniform across

the rotor and equal to $U_{r,h}$, whereas in the pitch case it is higher than $U_{r,h}$ in the upper portion of the rotor disk and lower in the lower portion. If we compare cases of surge and pitch motions with similar $U_{r,h}$, the mean power is slightly higher in case of pitch motion and this is attributed to the higher amplitude of wind speed oscillations in the upper part of the rotor. The increment of generated power with surge motion is similar for the two wind turbines. For a pitch motion of equal amplitude, $U_{r,h}$ is higher for the 15 MW than for the 5 MW, thus the 15 MW reaches a higher maximum power.
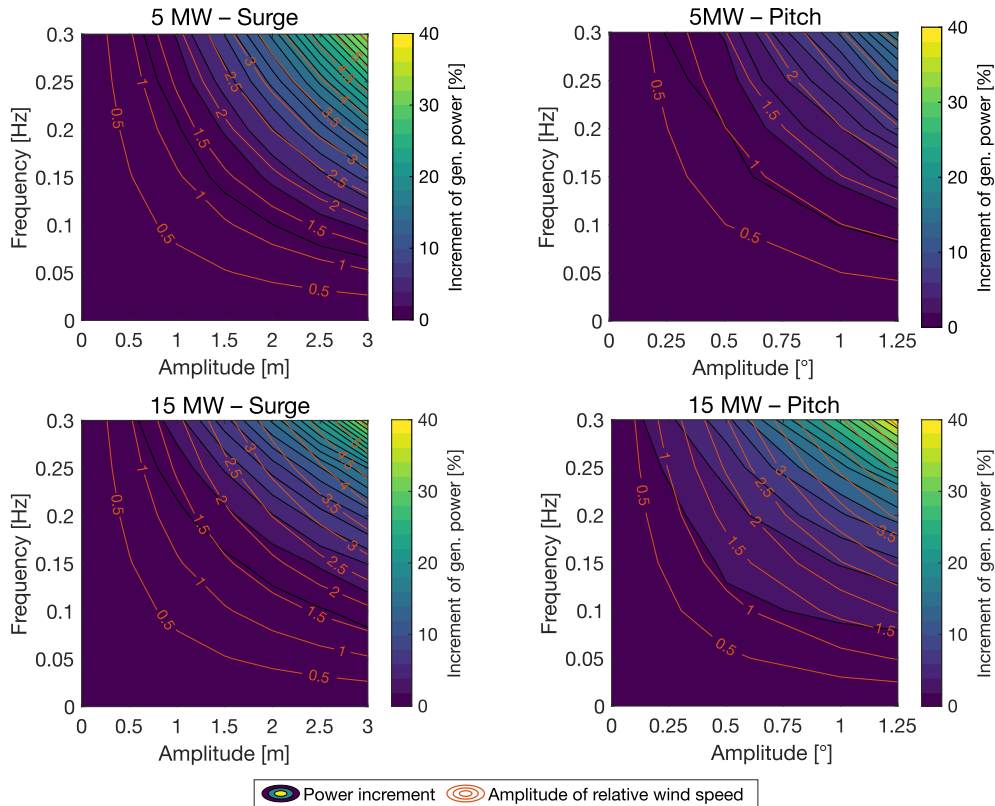

Figure 11. Increment of average generated power of the NREL 5 MW and of the IEA 15 MW with prescribed motion in the platform surge and pitch directions and a below rated wind speed of 9 m/s. The generated power is normalized by the turbine power with no prescribed motion. The "amplitude of relative wind speed" is the amplitude of the apparent wind speed at hub due to platform motion ($U_{r,h}$).

$\overline{P_g}$ in the above rated region is slightly lower than the rated power regardless of the tower base motion. Variations in generated power due to harmonic motion in the sway, heave, roll, and yaw directions are between -0.3% and +0.4% with a wind speed of 9 m/s.

Harm-M simulations show a wind turbine operating at a below-rated wind speed produces more power if the rotor moves cyclically in the wind direction and the increment is due to the energy in the apparent wind. This is in agreement with the analytical model of Eq. 3 and with results of Amaral et al. (2022) and Cottura et al. (2022) obtained with comparable approaches. According to results of the Harm-M simulations, platform motion driven by wave excitation can bring a meaningful

increment of the generated power. However, with Harm-W, Coupled-S and Coupled-C simulations we will show these gains are not achieved in normal operating conditions.

3.4 Power response with regular waves

Figure 12 shows $\overline{P_\mathrm{g}}$ for the four platforms with wind and waves aligned to the platform main axis and a wind speed of 9 m/s. We see wave excitation increases the generated power in all platforms, the 5 MW spar has the largest increment and the 15 MW semi-submersible has the smallest. In all turbines the power increment is proportional to wave amplitude. In first approximation, platform motion due to wave excitation is linearly proportional to wave height, therefore, bigger waves result in greater movements in the along-wind direction, subsequently leading to higher mean power output with the mechanism explained in Eq. 3 and with the Harm-M simulations.
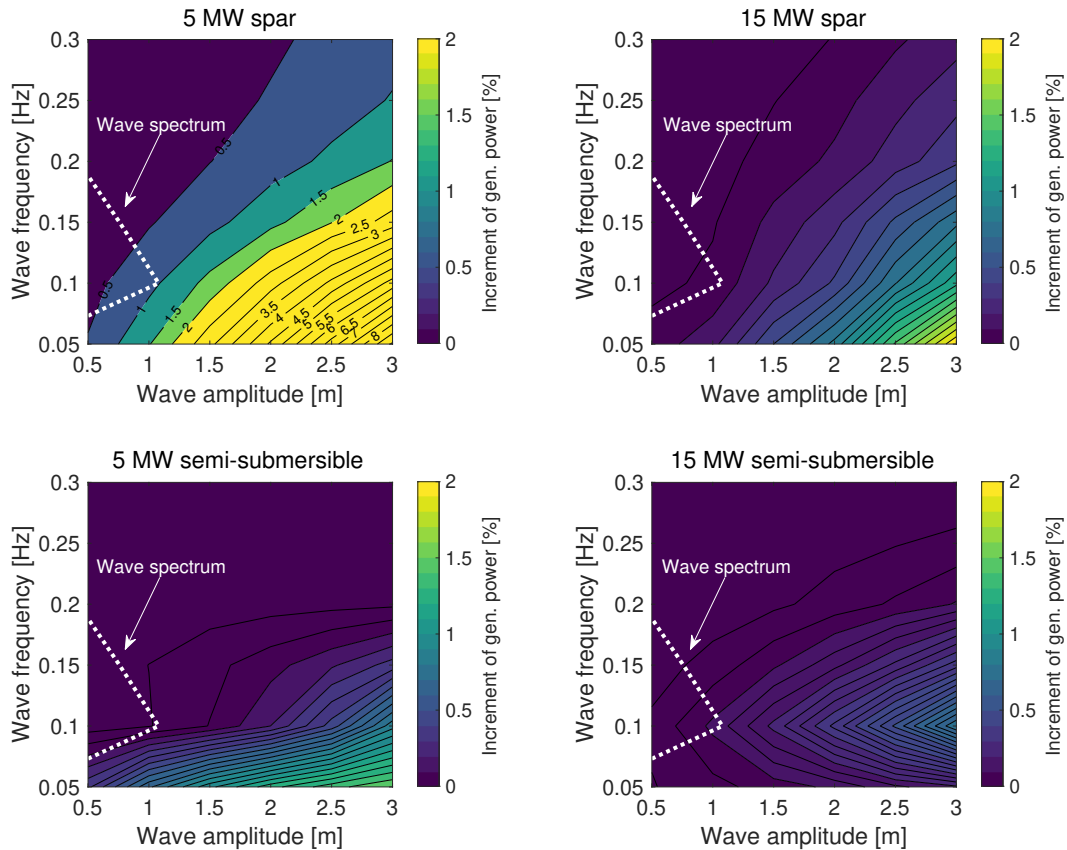

Figure 12. Increment of average generated power of the four floating wind turbines with wind and waves aligned to the platform main axis and a below rated wind speed of 9 m/s. The generated power is normalized by the turbine power with no waves. The dotted line is in correspondence of the wave spectrum with $H_\mathrm{s} = 4$ m and $T_\mathrm{p} = 9$ s. The increment of generated power for the 5 MW spar is above 2%, which is the upper limit for the other three floating wind turbines, and is indicated by labels on contours lines.

345　Except for the VolturnUS, the power increment is inversely proportional to wave frequency for a given wave amplitude. This result, which appears to be in contradiction with Harm-M results, is justified when taking into account the dynamic response to wave excitation of the platforms. Lower-frequency waves excite the FOWTs closer to their natural frequencies, resulting in larger movements. In the 15 MW semi-submersible case, the maximum power increment is found at 0.1 Hz due to the platform hydrodynamic characteristics.

350　In the Harm-W analysis, the 5 MW spar wind turbine has the largest increment of generated power that reaches almost 10% with a wave amplitude of 3 m at 0.05 Hz. This large increment, which is not seen in other platforms, is likely due to the coupled surge and pitch motions that occur at relatively high frequency and involve large movements. The surge motion with 3 m waves of 0.05 Hz frequency is over 3 m of amplitude for the 5 MW spar, whereas it is lower than 1 m in all other turbines. Comparing the increment of $\overline{P_g}$ for the two turbine sizes and for the same floater type, we see that power gains for the 5 MW turbines are

355　generally higher than for their 15 MW counterparts. This is due to the fact that platform modes are at lower frequency in the 15 MW FOWTs and motion due to first-order wave loads is milder.

Figure 12 shows that large-amplitude low-frequency waves can increase the power output of floating wind turbines. However, these power gains are achieved in a real scenario if waves with these characteristics exist. The dashed region in Fig. 12 is in correspondence of a wave spectrum that can occur at the Golf de Fos site. The wave spectrum is obtained from the wave height PSD computed according to the JONSWAP model of Hasselmann et al. (1973) with $H_s = 4$ m and $T_p = 9$ s. This is the most

360　severe sea state recorded in the dataset at our disposal and has rather high waves of low period, which is the condition required to increase power production. As visible, wave excitation is not powerful enough to generate a meaningful increase of the generated power. Depending on the installation site, it is possible that during its lifetime the floater may encounter a harsher sea, but the probability of occurrence at wind speeds lower than rated is generally low.

365　To investigate the influence of wind-wave directionality, we calculated $\overline{P_g}$ of the four floating wind turbines for a below rated wind speed of 9 m/s, regular waves of 0.1 Hz, and wave coming-from direction $\beta = [0°, 30°, 60°, 90°, 120°]$, while $\varphi = \theta = 0°$ always. The results are reported in Fig. 13: the largest power output gain is always achieved when wind and waves are aligned, because wave forces the platform to move in the wind direction. Conversely, when wave is perpendicular to wind, motions in the sway and roll directions are excited and these have a negligible effect on the generated power. When waves are

370　perpendicular to the platform main axis ($\gamma = 90°$) the increment of $\overline{P_g}$ is minimum and close to zero. The trend is confirmed for three values of wave amplitude and a similar result is obtained with waves of 0.05 Hz frequency (not shown here for brevity).

Simulations with the Harm-M and the Harm-W models demonstrate it is necessary to have large-amplitude along-wind motions to increase the mean generated power. However, in normal operating conditions it is unlikely to achieve these gains. The large-motions condition conflicts with the current design practice of floaters and wind turbines, which tries to place the

375　structure natural frequencies away from the wave spectrum to reduce mechanical loads, reduce the material usage and increase the machine fatigue life.
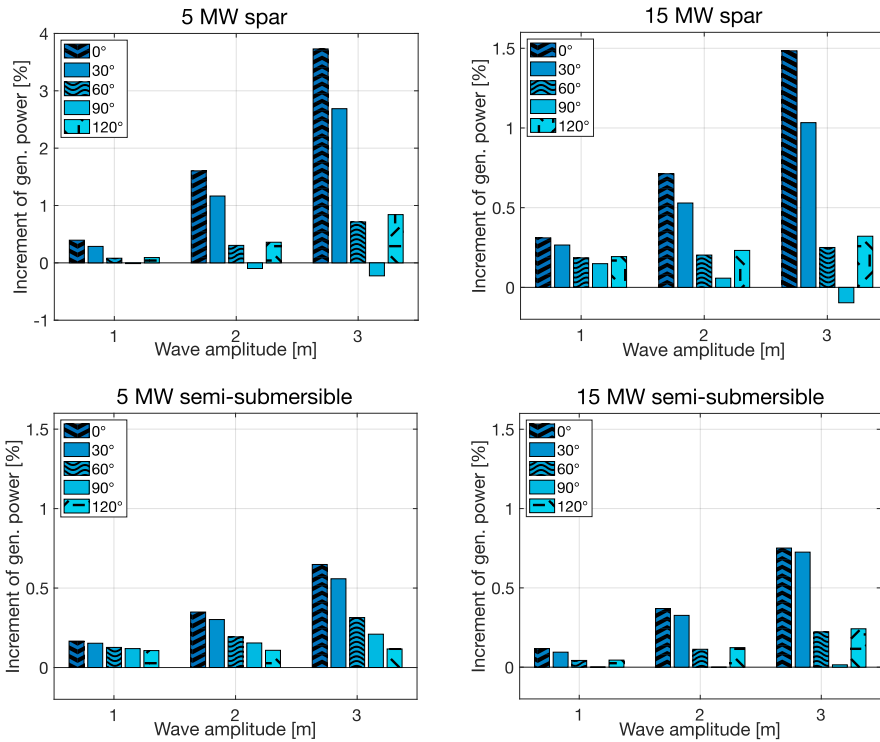
Figure 13. Increment of generated power of the four floating wind turbines due to harmonic waves with a below rated wind speed of 9 m/s, regular waves of 0.1 Hz frequency and five values of the misalignment angle γ.

3.5 Power response with stochastic wind and waves

A full picture of the energy conversion process of a floating wind turbine is gained with the Coupled-S and Coupled-C simulations which consider realistic stochastic wind and waves. In our study, the Coupled-C scenario is the most faithful representation of the environmental conditions of the studied sea area since it reproduces the mutual relationship between wind and waves based on recorded met-ocean data. The key parameter we use to understand the impact of waves on the wind turbine power production in Coupled-S and Coupled-C scenarios is the AEP presented in Sect. 3.5.2. Before discussing the AEP estimates, in Sect. 3.5.1 we delve into the physics of the power generation process: we examine the effect of wave excitation and wind-wave misalignment on the changes in wind turbine power and on the rotor local inflow.

3.5.1 Wind turbine power and rotor local inflow

Figure 14 shows the variation of generated power of the four floating wind turbines in the Coupled-S and Coupled-C scenarios with respect to the steady-wind no-wave cases of Fig. 7. To emphasize the effect of wind turbulence alone on the generated power, we introduce a case with a fixed foundation and turbulent wind ($I_{\mathrm{ref}} = 0.12$) to our comparison.

In all four FOWTs, the effect of wind turbulence is to increase power at low wind speeds and to decrease it around rated, as seen in Fig. 9. This trend is similar with waves and the power generated in cases with wind-wave misalignment of any amount is similar to the cases with aligned wind and waves.
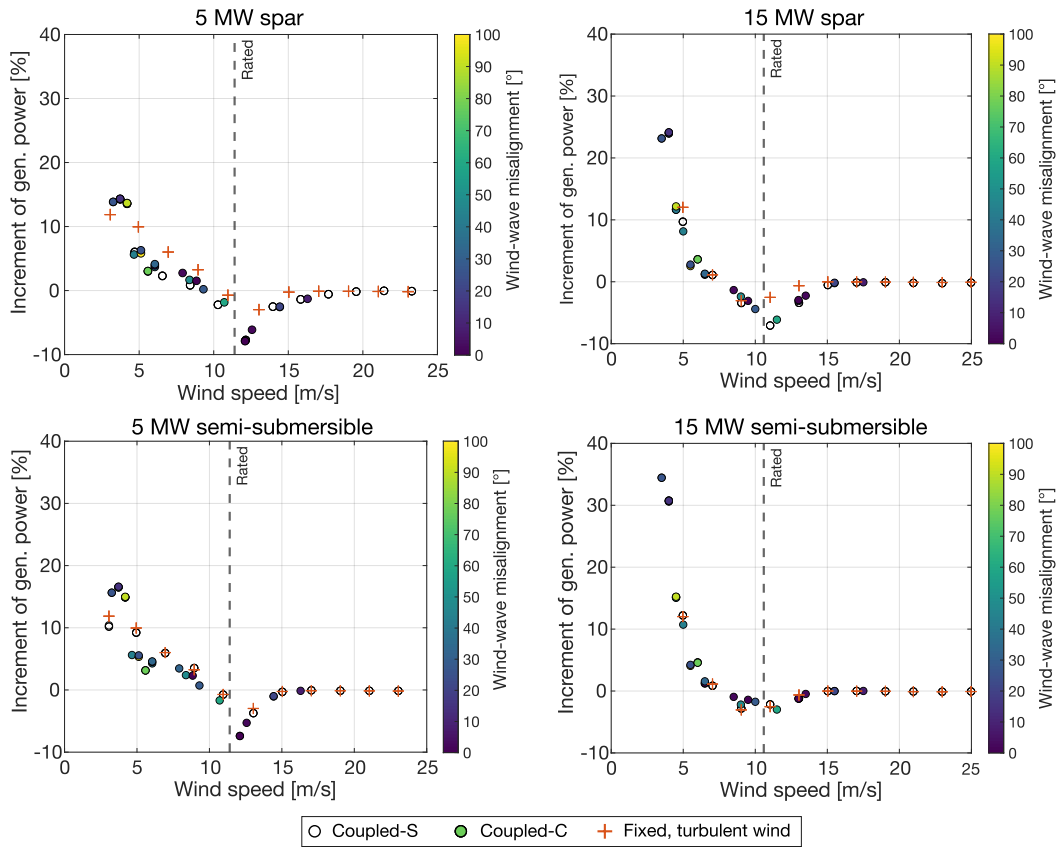

Figure 14. Increment of average generated power of the four floating wind turbines in the Coupled-S and Coupled-C scenarios with respect to the steady-wind no-wave cases. Markers of the Coupled-C cases are colored according the absolute value of wind-wave misalignment angle $|\gamma|$. The "Fixed, turbulent wind" case is added to the comparison to show the effect of wind turbulence.

To clarify the impact of wind and waves on the energy conversion process occurring at the wind turbine rotor we examine the time series presented in Fig. 15. Specifically, we analyze the generated power (P_{g}) and rotor-averaged relative wind speed ($V_{\mathrm{r,avg}}$) of the four floating wind turbines under mean wind speeds of 5 m/s and 9 m/s that fall in the below rated region. In these wind conditions the wave spectrum has similar parameters in the Coupled-S and Coupled-C cases, but in the Coupled-C environment waves are not aligned to the wind direction (cfr. Table B1 and Table B2). The parameter $V_{\mathrm{r,avg}}$ is computed by averaging the local relative velocity at the blade sections used in the aerodynamic model of OpenFAST. It is an indicator of the energy available for the rotor to be converted in electric power and, as it is shown in Eq. 2-3 where $V_{\mathrm{r}} = V_{\mathrm{r,avg}}$, its fluctuating component may lead to increased generated power.
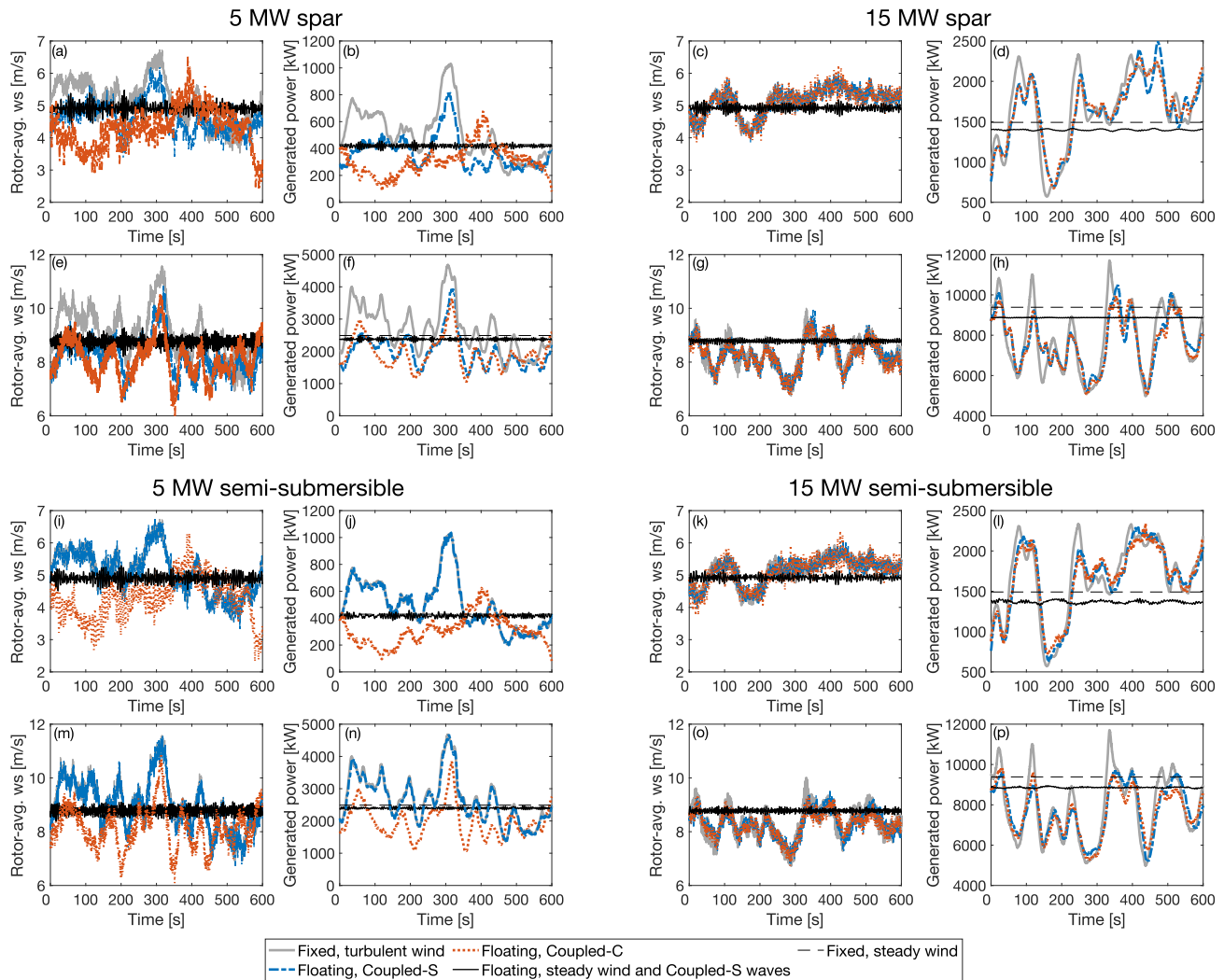
Figure 15. Effect of wind turbulence and waves on the power conversion process of the four floating wind turbines: time series of rotor-averaged wind speed and generated power. **(a), (b), (c), (d), (i), (j), (k), (l)** mean wind speed of 5 m/s. **(e), (f), (g), (h), (m), (n), (o), (p)** mean wind speed of 9 m/s.

400   In all four FOWTs, the average power with steady wind is lower with a floating foundation and waves than with a fixed foundation: the energy of waves is not enough to compensate for the reduction of rotor area projection due to the floating platform compliance. In cases with stochastic wind, $V_{r,avg}$ and P_g have low-frequency fluctuations one order of magnitude larger than those due to waves only. The impact of wind turbulence on the wind kinetic energy and hence on the generated power is dominant over the effect of waves.

405   At 5 m/s, wind fluctuations increase $\overline{P_g}$ that is higher than in the steady wind case, as already discussed in Fig. 9. This effect of turbulence vanishes for higher wind speeds and $\overline{P_g}$ of turbulent wind cases with a 9 m/s mean wind speed is slightly lower

than with steady wind. In all cases of Fig. 15 the average power generated with waves is slightly lower than with a fixed tower bottom. The 5 MW spar FOWT suffers the largest decrement because it has the largest platform tilt (e.g., at 9 m/s the 5 MW spar has a pitch rotation of 3° whereas the 5 MW semi-submersible has a pitch rotation of 1.2°).

3.5.2 Site-specific power curves and AEP

Information about power generated by the four floating wind turbines is summarized with site-specific power curves and AEP estimates that are computed with the algorithm described in Appendix C.

Figure 16 shows the site-specific power curves from Coupled-S and Coupled-C simulations of the four FOWTs and of the fixed tower bottom case. The fixed case has the same turbulent wind of the spar and semi-submersible cases and adopts the same control strategy of the floating wind turbines. The steady-state case of the fixed turbine with peak shaving, reported from Fig. 7, serves as a reference of the wind turbine performance when wind is modeled as uniform and steady.
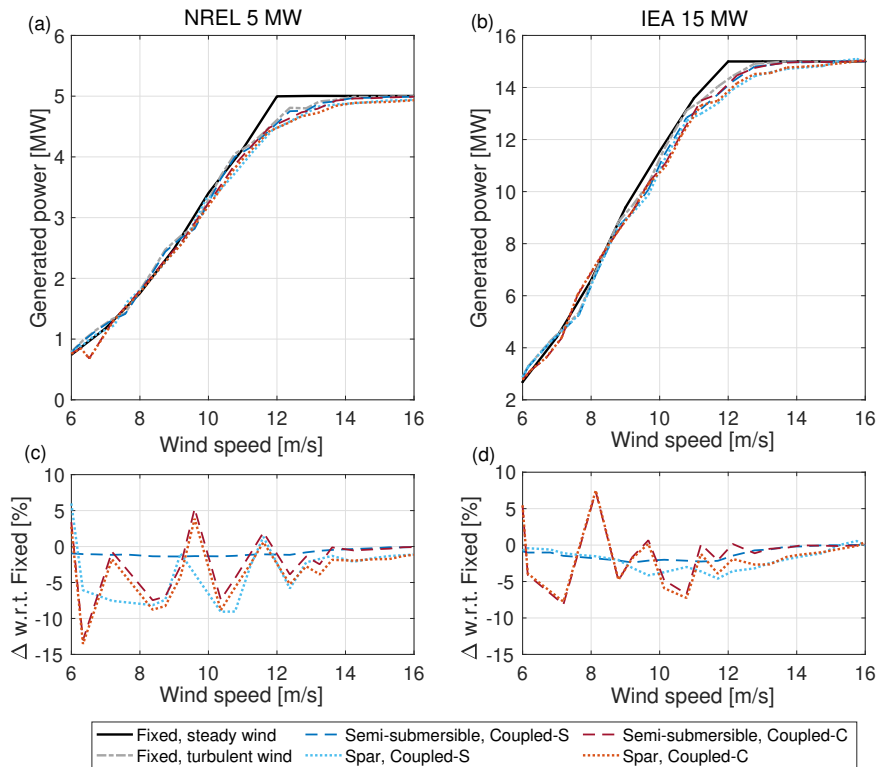

Figure 16. Site-specific power curves of the NREL 5 MW and IEA 5 MW wind turbines with a fixed, a semi-submersible, and a spar foundations. **(a), (b)** power curves obtained in Coupled-S and Coupled-C simulations with stochastic wind and irregular waves, except for the "Fixed steady-state" ones, which are reported from Fig. 7 as a reference of the turbine performance in steady wind. **(c), (d)** percent variations of the power generated in a floating case compared to a fixed tower-base case with turbulent wind.

23

With a floating foundation and stochastic waves the power curve is generally lower than in the fixed case, especially in the below rated region, and this is ascribed to the platform static tilt. Indeed, in Coupled-S simulations, the power loss with respect to the fixed case increases across the partial-load region with the same trend of the turbine thrust curve (see Fig. 3) and becomes negligible in the full-load region, where rotor thrust decreases and the turbine power is saturated at the wind turbine nameplate capacity. The largest decrement is in proximity of the rated wind speed, where the turbine is more sensitive to blade pitch.

The Coupled-C power curves deviate more from the fixed condition than those obtained in the Coupled-S simulations, especially in low wind speeds. In some wind speed bins, the Coupled-C power curves are above the fixed case, but this is attributed to the methodology for computing the site-specific power curve rather than the wind turbine response that is not expected to change suddenly in contiguous wind speed bins. Although we have not analyzed the sensitivity of the power curve to the number of clusters, we expect these oscillations to be smaller if the number of simulations is increased and if the environmental conditions are extracted from a larger dataset covering more uniformly the wind speed operating range of the wind turbines.

Interestingly, the two spar FOWTs reach the rated power at a higher wind speed than the semi-submersibles. This behavior is consistent in Coupled-S and Coupled-C simulations and it is ascribed to the nacelle-velocity feedback controller. Near the rated wind speed, the nacelle controller is activated to stabilize platform motion at the expense of a lower efficiency.

The AEP estimates of the four FOWTs with different modeling of wind and waves are reported in Fig. 17. In all cases the energy production with a floating foundation and waves is lower than in the fixed tower-bottom case. Simulations with regular waves show the increment of generated power due to wave-driven motion is around 0.1% for a typical wave spectrum and this small gain is not enough to offset the power loss due to platform tilt caused by thrust and platform compliance. The AEP obtained from simulations with wind-wave misalignment (Coupled-C) is close to the case with aligned wind and waves (Coupled-S). The small differences are attributed to the AEP estimation algorithm rather than a different physics of the power conversion process of the floating wind turbines, as already observed regarding the power curves of Fig. 16.

3.5.3   Concluding the analysis of results with stochastic wind and waves

We see that in realistic sea conditions the action of waves does not change significantly the power generated by the four floating wind turbines object of this study. Their energy yield is lower than a bottom-fixed wind turbine, in particular their power curve is reduced near the rated wind speed due to the platform static tilt. In realistic environmental conditions, the power output is driven by wind turbulence rather than waves.

Variations of the power curve due to uncertainty in the shear exponent and turbulence intensity are comparable to the power losses of a FOWT with respect to a bottom-fixed turbine. A recent study of Wiley et al. (2023) shows that turbulent wind speed standard deviation is the single parameter with the highest impact on rotor loads and global motions for the DeepCwind semi-submersible, confirming that a detailed knowledge of the wind environment is needed when assessing the response of floating wind turbines.

The dataset at our disposal covers a time span shorter than what is normally considered in the energy assessment of a wind power plant; wind speed values are low for an area generally seen as quite favorable for the development of floating wind
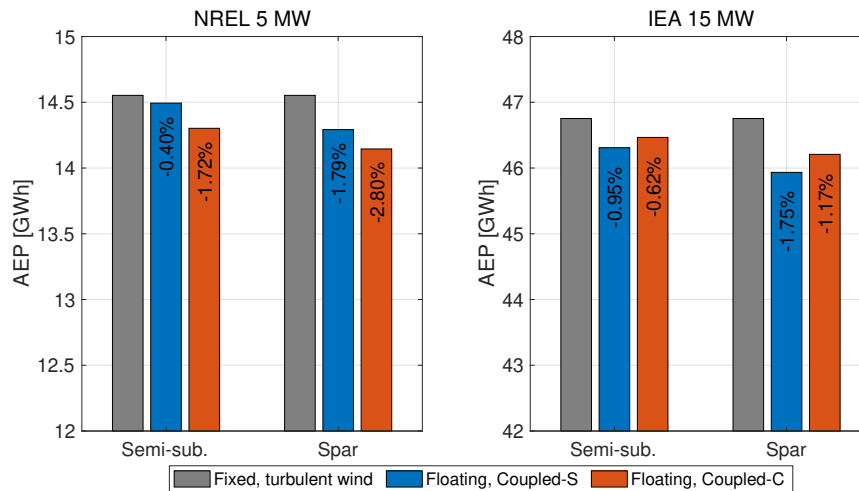
Figure 17. Annual energy production (AEP) of the NREL 5 MW and IEA 5 MW wind turbines obtained with a fixed foundation and turbulent wind, with semi-submersible and spar foundations from the Coupled-S and Coupled-C simulation scenarios. The percent variation of AEP with respect to the fixed case is reported on top of the bars.

projects, possibly due to the Marignane weather station being located onshore. This is likely to affect the AEP value that may underestimate the true energy potential of the sea site. However, our interest was primarily in understanding the impact of waves on energy production. The dataset covers a winter period when waves are generally stronger, thus conclusion are expected to be valid also if a larger dataset is analyzed.

4 Conclusions

A floating wind turbine rotor normally undergoes large movements permitted by the platform compliance and it may operate differently than with a fixed foundation with possible consequences on the energy capture. Moreover, waves introduce energy in the system forcing the floater to move which can potentially increase the generated power.

To understand how waves and platform dynamics impact the power production of a floating wind turbine we carried out multi-physics simulations of four FOWTs of 5-15 MW with spar and semi-submersible support structures. We used four simulation models of increasing complexity that gradually move from simple analytical calculations to a non-linear aero-servo-hydro-elastic model reproducing a realistic scenario with stochastic wind and waves in the Mediterranean Sea.

The main findings of this research are:

1. large along-wind motions can increase the rotor power, but these movements are prevented by the current design philosophy of semi-submersible and spar platforms;

2. the energy production of the floating wind turbines examined in this study is lower than for a fixed turbine in equal wind conditions;

25

3. wind modeling is more important than wave modeling for correct estimation of a floating wind turbine power production, at least for a site with met-ocean conditions similar to the one we considered here.

470   Concerning the first finding, we have shown that power gains due to wave-driven motions are possible only in below-rated winds speeds because above the rated wind speed power is saturated by the wind turbine controller. The increment in power is proportional to the amplitude and frequency of platform movement and it is maximum when the rotor moves in the along wind direction. Instead, with wind-wave misalignment, part of the wave energy is used to excite cross-wind motions that do not contribute to increasing the energy of the flow available for the rotor to be converted in electric power. Taking into account
475 the hydrodynamic loads the platform dynamic response we see wave excitation is generally not strong enough to achieve the large movements required to have a significant rise of generated power. Large, high-frequency movements are required to increase the power output of wind turbines. These are difficult to achieve because wind and wave forcing generally occurs at low frequencies and because large movements can only be achieved through resonance excitation of the platform modes, which would result in high structural loads. The large motion condition is in conflict with the design objectives of the platforms we
480 examined which aim to reduce material usage and extend as much as possible the fatigue life of the system.

    Concerning the second finding, the lower performance of a floating wind turbine compared to a bottom-fixed one is due to: the use of wind turbine control strategies that mitigate structural loads sacrificing energy conversion efficiency, wind turbulence and shear, and the static tilt of the floater caused by the combination of thrust force and high compliance of floating foundations. It should be verified if these results obtained for spar-buoy and semi-submersible wind turbines are also valid for tension-leg
485 platform (TLP) systems, which tend to have higher frequency and smaller amplitude motions.

    About the third finding, we realized that information about wind parameters, such as shear and turbulence, might be scarce in the early stage of floating wind projects and this lack of data should be addressed properly when evaluating the energy potential of a floating wind plant. At the same time, the energy evaluation process can be simplified considering a reduced number of wave conditions. Future work should prove if this is true also for sites characterized by different environmental parameters
490 (e.g., stronger waves).

    A wind turbine power curve is influenced significantly by the wind turbine control strategy and floater restoring characteristics which must be modeled in energy calculations. This is important for the individual machines, but also for wind farm modeling, where the power curve is often used in engineering tools as a simplified representation of the turbine response (e.g., in FLOw Redirection and Induction at Steady state FLORIS (NREL (2023b))).
495   As we have shown, exploiting the energy of waves with the current technology of semi-submersible and spar-buoy systems is not possible. Future designs may explore the trade-off between loads and increased power and see if it is feasible to leverage the peculiar physics of a floating rotor to harvest more energy and further decrease the cost of floating wind.

Data availability. The OpenFAST models and the results of simulations can be accessed via Fontanella et al. (2024).

Appendix A: Example of KMA clustering

500 The K-means algorithm introduced in Sect. 2.1.4 is applied to the dataset of the Golf de Fos site presented in Sect. 2.3 to extract $M = 5$ clusters. The number of clusters used in this example is lower than in Coupled-C simulations, where $M = 36$, to facilitate interpretation of the result.

Figure A1 shows the KMA output. Each dot is one of the 3362 conditions in the dataset represented in the five-dimensional space $\mathbf{x} = \{U, \beta, H_{\mathrm{s}}, T_{\mathrm{p}}, \theta\}$. Dots are colored according to the cluster to which they are assigned by the KMA. As visible, dots

505 of the same color share similar features, for example yellow dots are sea states with: $\beta = [250° - 50°]$, $\theta = [270° - 50°]$. In the KMA, each cluster is represented by its centroid, marked by a $\times$.
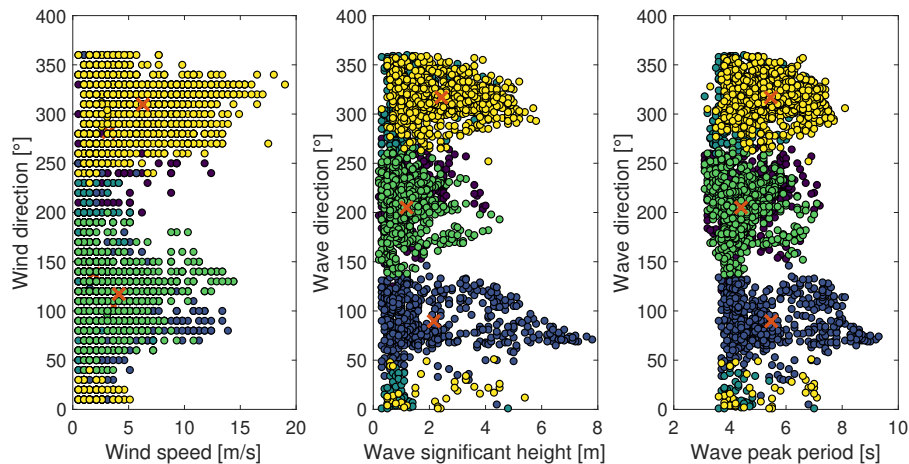

Figure A1. Met-ocean data (wind speed, wind direction, wave significant height, wave peak period, wave direction) of the Gulf de Fos site are divided into clusters with the K-means algorithm. Datapoints are colored according to the cluster to which they are assigned and clusters centroids are marked by the $\times$.

As we see, if the number of clusters is too low, as in this example, centroids do not represent accurately the dataset features. In the yellow cluster there is no distinction of wind speed, wave height or wave period, which span a large range and sometimes are quite far from those of the cluster centroid.

Appendix B: Wind and wave conditions from clustering

510

The environmental conditions of Coupled-S simulations are summarized in Table B1 and those of Coupled-C simulations in Table B2.

Table B1. Wind and wave conditions of the Coupled-S simulations ("w. s." is wind speed).

Case ID	Mean w. s. [m/s]	Wave height [m]	Wave period [s]
1	3.0	1.2	5.0
2	3.0	1.2	6.0
3	3.0	1.2	4.0
4	5.0	1.5	5.0
5	5.0	1.5	6.0
6	5.0	1.5	4.0
7	7.0	1.7	6.0
8	7.0	1.7	5.0
9	7.0	1.7	7.0
10	9.0	2.0	6.0
11	9.0	2.0	5.0
12	9.0	2.0	7.0
13	11.0	2.3	6.0
14	11.0	2.3	7.0
15	11.0	2.3	5.0
16	13.0	2.5	6.0
17	13.0	2.5	7.0
18	13.0	2.5	8.0
19	15.0	2.8	6.0
20	15.0	2.8	7.0
21	15.0	2.8	8.0
22	17.0	3.0	7.0
23	17.0	3.0	6.0
24	17.0	3.0	8.0
25	19.0	3.3	7.0
26	19.0	3.3	6.0
27	19.0	3.3	8.0
28	21.0	3.5	7.0
29	21.0	3.5	8.0
30	21.0	3.5	9.0
31	23.0	3.8	7.0
32	23.0	3.8	8.0
33	23.0	3.8	9.0
34	25.0	4.0	7.0
35	25.0	4.0	8.0
36	25.0	4.0	9.0

Table B2. Wind and wave conditions identified by means of K-means clustering and used for the Coupled-C simulations ("w. s." is wind speed, "Count" is the number of datapoints in each cluster).

Cluster ID	Mean w. s. [m/s]	Wind direction [°]	Wave height [m]	Wave period [s]	Wave direction [°]	Count [−]
1	3.0	137	0.8	4.0	273	69
2	3.0	257	1.0	4.2	342	65
3	3.0	11	1.6	4.8	298	55
4	3.0	148	0.7	4.4	79	38
5	3.5	256	0.6	3.7	229	77
6	3.5	268	0.9	4.4	172	70
7	4.0	203	1.2	4.9	209	63
8	4.0	141	0.7	4.1	118	50
9	4.0	269	1.1	4.2	302	60
10	4.0	352	1.4	4.6	337	96
11	4.0	317	1.3	4.6	239	50
12	4.5	71	0.9	4.3	135	55
13	4.5	75	1.2	4.8	82	27
14	4.5	118	1.5	5.0	71	70
15	4.5	127	0.6	3.9	168	98
16	4.5	343	6.0	8.2	74	24
17	5.0	348	3.6	6.4	32	42
18	5.5	350	3.3	6.2	324	46
19	5.5	85	1.4	4.7	225	124
20	6.0	135	1.4	4.7	213	111
21	6.0	313	1.4	4.6	310	142
22	6.0	93	0.9	4.1	191	105
23	6.5	316	2.9	5.9	313	49
24	6.5	310	1.5	4.7	351	68
25	6.5	74	3.8	7.1	108	102
26	8.5	104	1.8	5.2	107	73
27	9.0	273	1.6	5.3	224	53
28	9.5	270	2.1	5.5	269	50
29	10.0	284	1.9	5.0	313	123
30	11.5	126	1.4	4.5	186	47
31	13.0	86	5.3	7.8	85	114
32	13.0	298	3.0	5.9	315	127
33	13.5	319	2.1	5.2	316	28
34	15.5	280	4.1	6.8	302	49
35	15.5	141	2.9	5.9	178	56
36	17.5	325	3.9	6.6	316	135

Appendix C: Site-specific power curve and annual energy production

The site-specific power curve and the AEP are derived according to the algorithm of the IEC 61400-12 standard (International
515 Electrotechnical Commission (2022)) based on time series of hub-height wind speed and generated power.

Time series of wind speed and generated power are divided into 10 min segments and, for each segment, the mean value is
computed. The dataset of 10 min-mean values is sorted using the method of bins:

1. the wind speed range is divided in 0.5 m/s contiguous bins centered on multiples of 0.5 m/s and the dataset is distributed
   inside the bins according to the 10 min-mean wind speed;

520 2. the dataset must cover a wind speed range extending from 1 m/s below cut-in to 1.5 time the wind speed at 85% of the
   wind turbine rated power. Otherwise, for pitch-controlled wind turbines as the NREL 5 MW and the IEA 15 MW, the
   power curve is considered complete when the rated power is reached and the average power does not change by more
   than 0.5% of the power, or 5 kW, for three consecutive wind speed bins. If the power curve does not include data up to
   cut-out wind speed, the power curve is extrapolated from the maximum complete wind speed to cut-out wind speed;

525 3. the dataset is considered complete when each bin includes a minimum of 30 min of sampled data. For incomplete bins,
   the bin value is estimated by linear interpolation from the two adjacent complete bins.

The power curve (i.e., power as a function of wind speed) is determined based on the hub-height wind speed of each bin:

$$V_i = \frac{1}{N_i} \sum_{j=1}^{N_i} V_{n,i,j}, \tag{C1}$$

where V_i is the average wind speed in bin i, $V_{n,i,j}$ is the wind speed of the data point j in bin i, N_i is the number of 10 min
530 data points in the bin i. The power of each bin is:

$$P_i = \frac{1}{N_i} \sum_{j=1}^{N_i} P_{n,i,j}, \tag{C2}$$

where P_i is the average power in bin i, $P_{n,i,j}$ is the power of the data point j in bin i, N_i is the number of 10 min data points
in bin i. An example of power curve obtained with the method of bins is reported in Fig. C1.
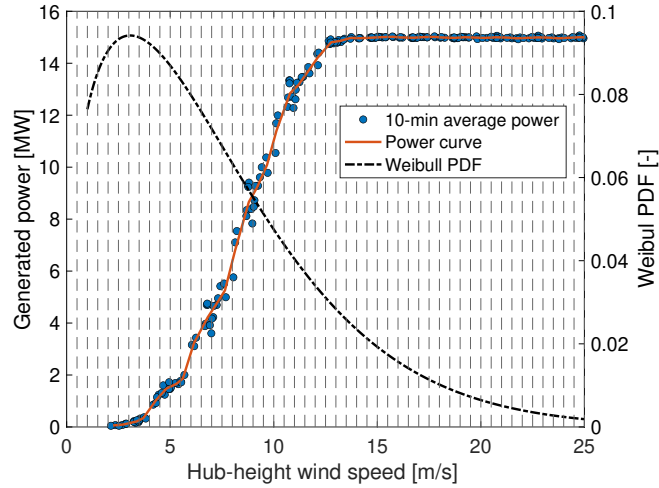
Figure C1. Construction of the site-specific power curve from simulations of the Coupled-S or Coupled-C scenarios. Time series of generated power obtained from OpenFAST simulations are divided into 10 min sub-histories and dots are the corresponding mean values.

The AEP is evaluated combining the power curve obtained with the method of bins with the wind speed frequency distribution as:

$$\text{AEP} = N_h \sum_{i=1}^{N} (F(V_i) - F(V_{i-1})) \left(\frac{P_{i-1} + P_i}{2} \right), \tag{C3}$$

Where AEP is the annual energy production, $N_h = 8760$ is the number of hours in one year, N is the number of bins, V_i is the average wind speed in bin i, P_i is the average power of bin i, $F(V_i)$ is the site-specific Weibull cumulative probability distribution function for wind speed (i.e., the one of Fig. 5 in the case of this paper). The summation in Eq. C3 is initiated setting $F(V_{i-1}) = V_i - 0.5$ and $P_{i-1} = 0$.

References

Abbas, N. J., Zalkind, D. S., Pao, L., and Wright, A.: A reference open-source controller for fixed and floating offshore wind turbines, Wind Energy Science, 7, 53–73, https://doi.org/10.5194/wes-7-53-2022, https://wes.copernicus.org/articles/7/53/2022/, 2022.

550   Allen, C., Viselli, A., Dagher, H., Goupee, A., Gaertner, E., Abbas, N., Hall, M., and Barter, G.: Definition of the UMaine VolturnUS-S Reference Platform Developed for the IEA Wind 15-Megawatt Offshore Reference Wind Turbine, Technical Report NREL/TP-5000-76773, https://www.nrel.gov/docs/fy20osti/76773.pdf, Available at https://www.nrel.gov/docs/fy20osti/76773.pdf, 2020.

Allen, C., Viselli, A., Dagher, H., Goupee, A., Gaertner, E., Abbas, N., Hall, M., and Barter, G.: UMaine VolturnUS-S Reference Platform, https://github.com/IEAWindTask37/IEA-15-240-RWT/tree/master/OpenFAST, 2023.

555   Amaral, R., Laugesen, K., Masciola, M., von Terzi, D., Deglaire, P., and Viré, A.: A frequency-time domain method for annual energy production estimation in floating wind turbines, Journal of Physics: Conference Series, 2265, 042 025, https://doi.org/10.1088/1742-6596/2265/4/042025, https://dx.doi.org/10.1088/1742-6596/2265/4/042025, 2022.

Arthur, D. and Vassilvitskii, S.: K-Means++: The Advantages of Careful Seeding, in: Proceedings of the Eighteenth Annual ACM-SIAM Symposium on Discrete Algorithms, SODA '07, p. 1027–1035, Society for Industrial and Applied Mathematics, USA, 2007.

560   Branlard, E., Shields, M., Anderson, B., Damiani, R., Wendt, F., Jonkman, J., Musial, W., and Foley, B.: Superelement reduction of substructures for sequential load calculations in OpenFAST, Journal of Physics: Conference Series, 1452, 012 033, https://doi.org/10.1088/1742-6596/1452/1/012033, https://dx.doi.org/10.1088/1742-6596/1452/1/012033, 2020.

Campos, A., Molins, C., Gironella, X., and Trubat, P.: Spar concrete monolithic design for offshore wind turbines, Proceedings of the Institution of Civil Engineers - Maritime Engineering, 169, 49–63, https://doi.org/10.1680/jmaen.2014.24, https://doi.org/10.1680/jmaen.565   2014.24, 2016.

Camus, P., Mendez, F. J., Medina, R., and Cofiño, A. S.: Analysis of clustering and selection algorithms for the study of multivariate wave climate, Coastal Engineering, 58, 453–462, https://doi.org/https://doi.org/10.1016/j.coastaleng.2011.02.003, https://www.sciencedirect.com/science/article/pii/S0378383911000354, 2011.

Clifton, A., Daniels, M. H., and Lehning, M.: Effect of winds in a mountain pass on turbine performance, Wind Energy, 17, 1543–1562, 570   https://doi.org/https://doi.org/10.1002/we.1650, https://onlinelibrary.wiley.com/doi/abs/10.1002/we.1650, 2014.

Cottura, L., Caradonna, R., Novo, R., Ghigo, A., Bracco, G., and Mattiazzo, G.: Effect of pitching motion on production in a OFWT, Journal of Ocean Engineering and Marine Energy, 8, 319 – 330, https://doi.org/10.1007/s40722-022-00227-0, https://www.scopus.com/inward/record.uri?eid=2-s2.0-85132638963&doi=10.1007%2fs40722-022-00227-0&partnerID=40&md5=ad3684f562590d9cf27f6c7ca5c64a95, 2022.

575   EMODnet: EMODnet Bathymetry World Base Layer, https://emodnet.ec.europa.eu/en/bathymetry, 2023.

Fleming, P. A., Peiffer, A., and Schlipf, D.: Wind Turbine Controller to Mitigate Structural Loads on a Floating Wind Turbine Platform, Journal of Offshore Mechanics and Arctic Engineering, 141, 061 901, https://doi.org/10.1115/1.4042938, https://doi.org/10.1115/1.4042938, 2019.

Fontanella, A., Colpani, G., De Pascali, M., Muggiasca, S., and Belloli, M.: OpenFAST models and simulation outputs to assess the impact 580   of waves and platform dynamics on floating wind turbine energy production, https://doi.org/10.5281/zenodo.10513599, https://doi.org/10.5281/zenodo.10513599, 2024.

France, M.: Mètéo-France. Gulf de Lion buoy, https://donneespubliques.meteofrance.fr/?fond=produit{&}id{_}produit=95{&}id{_}rubrique=32, 2022.

Gaertner, E., Rinker, J. and. Sethuraman, L., Zahle, F., Anderson, B., Barter, G., Abbas, N., Meng, F., Bortolotti, P., Skrzypinski, W.,
585   Scott, G., Feil, R., Bredmose, H., Dykes, K., Shields, M., Allen, C., and Viselli, A.: Definition of the IEA 15-Megawatt Offshore Ref-
       erence Wind Turbine, Tech. rep., National Renewable Energy Laboratory, https://www.nrel.gov/docs/fy20osti/75698.pdf, Available at
       https://www.nrel.gov/docs/fy20osti/75698.pdf, 2020.

       Hall, M. and Goupee, A.: Validation of a lumped-mass mooring line model with DeepCwind semisubmersible model test data, Ocean Engi-
       neering, 104, 590–603, https://doi.org/https://doi.org/10.1016/j.oceaneng.2015.05.035, https://www.sciencedirect.com/science/article/pii/
590   S0029801815002279, 2015.

       Hasselmann, K. F., Barnett, T. P., Bouws, E., Carlson, H. C., Cartwright, D. E., Enke, K., Ewing, J. A., Gienapp, H., Hasselmann, D. E.,
       Kruseman, P., Meerburg, A., Müller, P. M., Olbers, D. J., Richter, K., Sell, W., and Walden, H.: Measurements of wind-wave growth and
       swell decay during the Joint North Sea Wave Project (JONSWAP), 1973.

       International Electrotechnical Commission: Wind energy generation systems - Part 3-1: Design requirements for fixed offshore wind turbines,
595   IEC 61400-3-1:2019, Tech. Rep. IEC 61400-12-1:2022, International Electrotechnical Commission, https://webstore.iec.ch/publication/
       29360, 2019.

       International Electrotechnical Commission: Wind energy generation systems - Part 12-1: Power performance measurements of electricity
       producing wind turbines, IEC 61400-12-1:2022, Tech. Rep. IEC 61400-12-1:2022, International Electrotechnical Commission, https:
       //webstore.iec.ch/publication/68499#additionalinfo, 2022.

600   Jonkman, B., Mudafort, R. M., Platt, A., Branlard, E., Sprague, M., Jonkman, J., Ross, H., Hall, M., Vijayakumar, G., Buhl, M., Bortolotti, P.,
       Ananthan, S., Schmidt, M., Rood, J., Damiani, R., Mendoza, N., Shaler, K., Housner, S., Bendl, K., Carmo, L., Quon, E., Phillips, M. R.,
       Kusuno, N., and Salcedo, A. G.: OpenFAST/openfast: v3.4.1, https://doi.org/10.5281/zenodo.7632926, https://doi.org/10.5281/zenodo.
       7632926, 2023.

       Jonkman, B. J.: Turbsim User's Guide: Version 1.50, https://doi.org/10.2172/965520, https://www.osti.gov/biblio/965520, 2009a.

605   Jonkman, J.: Definition of the Floating System for Phase IV of OC3, NREL/TP-500-47535, https://www.nrel.gov/docs/fy10osti/47535.pdf,
       Available at https://www.nrel.gov/docs/fy10osti/47535.pdf, 2009b.

       Jonkman, J., Butterfield, S., Musial, W., and Scott, G.: Definition of a 5-MW reference wind turbine for offshore system development,
       NREL/TP-500-38060, https://www.nrel.gov/docs/fy09osti/38060.pdf, Available at https://www.nrel.gov/docs/fy09osti/38060.pdf, 2009.

       Krieger, A., Ramachandran, G. K. V., Vita, L., Alonso, P. G., Almeria, G. G., Berque, J., and Aguirre, G.: D7.2 Design Basis, LIFES50+
610   Deliverable, https://lifes50plus.eu/wp-content/uploads/2015/11/D72_Design_Basis_Retyped-v1.1.pdf, 2015.

       Mahfouz, M. Y., Molins, C., Trubat, P., Hernández, S., Vigara, F., Pegalajar-Jurado, A., Bredmose, H., and Salari, M.: Response of the
       International Energy Agency (IEA) Wind 15 MW WindCrete and Activefloat floating wind turbines to wind and second-order waves,
       Wind Energy Science, 6, https://doi.org/10.5194/wes-6-867-2021, https://wes.copernicus.org/articles/6/867/2021/, 2021.

       Martini, M., Guanche, R., Armesto, J. A., Losada, I. J., and Vidal, C.: Met-ocean conditions influence on floating offshore wind farms power
615   production, Wind Energy, 19, 399–420, https://doi.org/https://doi.org/10.1002/we.1840, https://onlinelibrary.wiley.com/doi/abs/10.1002/
       we.1840, 2016.

       Meteostat: Marseille - Marignane weather station, https://meteostat.net/en/station/07650?t=2023-06-12/2023-06-19, 2022.

       Molins, C., Trubat, P., and Mahfouz, M. Y.: UPC - WINDCRETE OpenFAST model 15MW FOWT - Grand Canary Island,
       https://doi.org/10.5281/zenodo.4322446, https://doi.org/10.5281/zenodo.4322446, 2020.

620   NREL: ROSCO. Version 2.8.0, https://github.com/NREL/ROSCO, 2023a.

       NREL: FLORIS, https://github.com/NREL/floris, 2023b.

Renan dos Santos, C., Abdelmoteleb, S.-E., Mendoza, A. S. E., and Bachynski-Polić, E. E.: Control Considerations for Very Large Floating Wind Turbines, IFAC-PapersOnLine, 55, 166–171, https://doi.org/https://doi.org/10.1016/j.ifacol.2022.10.426, https://www.sciencedirect.com/science/article/pii/S2405896322024727, 14th IFAC Conference on Control Applications in Marine Systems, Robotics, and Vehicles CAMS 2022, 2022.

Robertson, A., Jonkman, J., Masciola, M., Song, H., Goupee, A., Coulling, A., and Luan, C.: Definition of the Semisubmersible Floating System for Phase II of OC4, NREL/TP-5000-60601, https://www.nrel.gov/docs/fy14osti/60601.pdf, Available at https://www.nrel.gov/docs/fy14osti/60601.pdf, 2014.

Schelbergen, M., Kalverla, P. C., Schmehl, R., and Watson, S. J.: Clustering wind profile shapes to estimate airborne wind energy production, Wind Energy Science, 5, 1097–1120, https://doi.org/10.5194/wes-5-1097-2020, https://wes.copernicus.org/articles/5/1097/2020/, 2020.

St. Martin, C. M., Lundquist, J. K., Clifton, A., Poulos, G. S., and Schreck, S. J.: Wind turbine power production and annual energy production depend on atmospheric stability and turbulence, Wind Energy Science, 1, 221–236, https://doi.org/10.5194/wes-1-221-2016, https://wes.copernicus.org/articles/1/221/2016/, 2016.

van der Veen, G. J., Couchman, I. J., and Bowyer, R. O.: Control of floating wind turbines, in: 2012 American Control Conference (ACC), pp. 3148–3153, https://doi.org/10.1109/ACC.2012.6315120, 2012.

van Kuik, G. A. M., Peinke, J., Nijssen, R., Lekou, D., Mann, J., Sørensen, J. N., Ferreira, C., van Wingerden, J. W., Schlipf, D., Gebraad, P., Polinder, H., Abrahamsen, A., van Bussel, G. J. W., Sørensen, J. D., Tavner, P., Bottasso, C. L., Muskulus, M., Matha, D., Lindeboom, H. J., Degraer, S., Kramer, O., Lehnhoff, S., Sonnenschein, M., Sørensen, P. E., Künneke, R. W., Morthorst, P. E., and Skytte, K.: Long-term research challenges in wind energy – a research agenda by the European Academy of Wind Energy, Wind Energy Science, 1, 1–39, https://doi.org/10.5194/wes-1-1-2016, https://wes.copernicus.org/articles/1/1/2016/, 2016.

Vanelli, T., Rinker, J., and Zalkind, D. S.: Aeroservoelastic stability of a floating wind turbine, Journal of Physics: Conference Series, 2265, 042 001, https://doi.org/10.1088/1742-6596/2265/4/042001, https://dx.doi.org/10.1088/1742-6596/2265/4/042001, 2022.

Wiley, W., Jonkman, J., Robertson, A., and Shaler, K.: Sensitivity Analysis of Numerical Modeling Input Parameters on Floating Offshore Wind Turbine Loads, Wind Energy Science Discussions, 2023, 1–35, https://doi.org/10.5194/wes-2023-49, https://wes.copernicus.org/preprints/wes-2023-49/, 2023.

Wiser, R., Rand, J., Seel, J., Beiter, P., Baker, E., Lantz, E., and Gilman, P.: Expert elicitation survey predicts 37% to 49% declines in wind energy costs by 2050, Nature Energy, 6, 555–565, https://doi.org/https://doi.org/10.1038/s41560-021-00810-z, https://doi.org/10.1038/s41560-021-00810-z, 2021.